Pulsar Wind Nebulae: observations and models of 3C58 and discovery of superefficiency

Tingting Lin

Universitat Autònoma de Barcelona

Pulsar Wind Nebulae: observations and models of 3C58 and discovery of superefficiency

Ph.D. Dissertation

Tingting Lin

December 2020

Supervisor: Diego F. Torres

Tutor: LLuís Font Guiteras – Mentor: Aldo Serenelli

Universitat Autònoma de Barcelona
Departament de Física

Institute of Space Sciences (ICE, CSIC)

c. Can Magrans s/n, 08193 Bellaterra (Barcelona)

Contents

List of Figures

List of Tables

Chapter 1

Introduction

1.1 This thesis

This thesis is presented in the 'Paper Format' as described by the Universtitat Autònoma de Barcelona. This format implies that everything contained in the thesis has been published by the author in peer-reviewed astrophysical journals already. This allows for a much more focused presentation, where essentially only published results form part of the thesis, with an introduction giving the argument line and the basic context. This thesis is based on three related papers on the physics of pulsar wind nebulae that I did with my supervisor and a reduced number of colleagues. Of course, none of the latter colleagues is presenting (as has been properly, and formally declared) the same material to opt to any academic degree.

The three papers in which the following chapters of this thesis are based are,

1. Observing and modeling the gamma-ray emission from the pulsar/pulsar wind nebula complex PSR J0205+6449 – 3C 58 [astro-ph/1803.10863]
   J. Li, D. F. Torres, *T. Lin*, M.-H. Grondin, M. Kerr, M. Lemoine-Goumard, & E. de Ona Wilhelmi
   The Astrophysical Journal 858, article id. 84, 7 pp. (2018)

2. Discovery and Characterization of Superefficiency in Pulsar Wind Nebulae [astro-ph:1808.10613]
   D. F. Torres & *T. Lin*
   The Astrophysical Journal Letters 864, article id. L2 (2018)

3. Towards observing reverberating and superefficient pulsar wind nebulae [astro-ph/1903.68681]
   D. F. Torres, *T. Lin*, & F. Coti Zelati
   Monthly Notices of the Royal Astronomical Society 486, 1019-1033 (2019)

correspondingly, they are presented in Chapters 2, 3 and 4 of the thesis. They are also available in the online archive ArXiv (astro-ph), for which the numbers are given above.

Whereas each of the chapters present their introduction and conclusions on their own, the topical connection among them is clear already from the title. The first of the papers above considers the case of the complex formed by the pulsar / pulsar wind nebula (PWN) PSR J0205+6449 / 3C 58, especial due to its young age, significant power, and similarity to Crab (the best studied PWN). In this paper, my colleagues and I presented the results of the analysis of 8 years of *Fermi*-LAT data. The main aspect is that using a contemporaneous ephemeris for the pulsation, we could gate-off the pulsar (similarly to shutting it down, with the price of loosing a significant number of photons) and present a detailed analysis of PSR J0205+6449 both during its off-peak and on-peak phase intervals. We found that 3C 58 is significantly detected during the off-peak phase interval, and show that this is most likely produced by a pulsar wind nebulae. Differently from Crab, possible high-energy flares from 3C 58 were searched for, but none was unambiguously identified. I was in charge of analyzing the observed data in the context of a time-dependent model of pulsar wind nebulae based on the code TIDE (described below). I was also in charge of the comparison with previous models, as well as of the writing of a significant portion of the paper. It is supposed -and our model so confirms- that the PWN 3C 58 is not yet reverberating (has not yet been hit by the reverse shock of the supernova remnant). Thus, to study further the evolution of pulsar wind nebulae, older PWNe, or the same PWNe but evolved into the future, have to be considered. This is what we do in the next chapters.

The second paper, which I consider to be my main contribution, deals with the discovery and characterization of superefficiency in pulsar wind nebulae. This concept has been earlier entertained in a paper by Torres, when trying to explain the first observation of a magnetar nebula. The latter had a quite abnormal (higher than usual) 10% of efficiency in X-rays (i.e., 10% of the spin-down power would end up released in a small energy range around 1 keV, when usually this is about 2% or less). Superefficiency in pulsar wind nebulae is a short period in the evolution of the PWN, which, due to its compression because of the returning reverse shock of the supernova explosion, is characterized by an adiabatic heating of the nebula. The fact that there was such adiabatic heating (similar to the adiabatic cooling when it expands) was known since long (see chapter 3 references for details). But what was not clear was what would happen with the luminosities of the PWN at different energy ranges.

Due to the compression, the magnetic field of the PWN also increases, and thus the emission via synchrotron does too. Additionally, due to the adiabatic heating, there are more particles at higher energies than there were previously. Thus we have more particles, subject to a more intense field. Synchrotron luminosities would then quickly increase. I found, together with my supervisor, that such process can in fact produce PWN that for a short time are more luminous in X-rays and other frequencies, that what they have as

rotational energy at the time. The former is not a paradox, and should not be confused with the unphysical situation of energy not being conserved, but simple the consequence of the fact that the rotational spinning down of the pulsar is no longer the energy reservoir of the system. The reverse shock is providing extra energy to heat up particles and increase the field, that the spin-down power plays no role (I found) in limiting luminosities. This process does not last long, and depends on a number of physical parameters. It ends when the magnetic field pressure, increased because of the magnetic field, significantly risen up, is able to detain the kinematic pressure provided by the reverse shock. The PWN then re-expands, and eventually enters a phase a calmed expansion, which we model using Sedov. In this Sedov phase, the pressure-driven expansion can be regarded as adiabatic, the cooling timescales are much longer than dynamical timescales, so the cooling of the gas is only due to the expansion. For this second paper contained in chapter 3, I added several routines to the PWN evolutionary code TIDE, which I briefly introduce below, and that would allow me to compute the luminosity at a given energy range as a function of time, tracking at once all dynamical and pulsar-intrinsic properties.

Finally, the third paper, contained in Chapter 4, connects with the former rather directly and I also consider it to be part of the backbone of my work these years. In it, I numerically study the radiative properties of the reverberation phase of PWNe in general. To achieve this I took, on the one hand, several well-characterized PWNe and used them as examples to study how would they react to the reverse shock hitting. On the other hand, I explored a broad range of PWN models defined appropriately using the $P\dot{P}$ diagram (introduced below) to study their reverberation and superefficiency phases in a systematic way. Having attained such modelling, I estimated via Monte Carlo simulations how many Galactic PWNe are expected to be reverberating or in a superefficiency stage at any given time, providing the first such estimations, and realized predictions for possible future detections with the next generation of X-ray satellites and ground-based experiments. In this paper I was in charge of producing the sample of pulsars to analyze, both synthetic and corresponding to the particular PWNe analyzed (such as PWN G54, G21, and others), providing simulations for all, and reducing them to understand the superefficiency feature. I collaborated in the simple populations synthesis done to understand the frequency of PWNe expected to be in contracting phases as well.

In the remaining of this chapter, I step back to introduce the basic concepts of pulsar and pulsar wind nebulae that my papers use next. Some of them will be briefly re-introduced as in the original papers, to facilitate the flow of the next chapters, when needed.

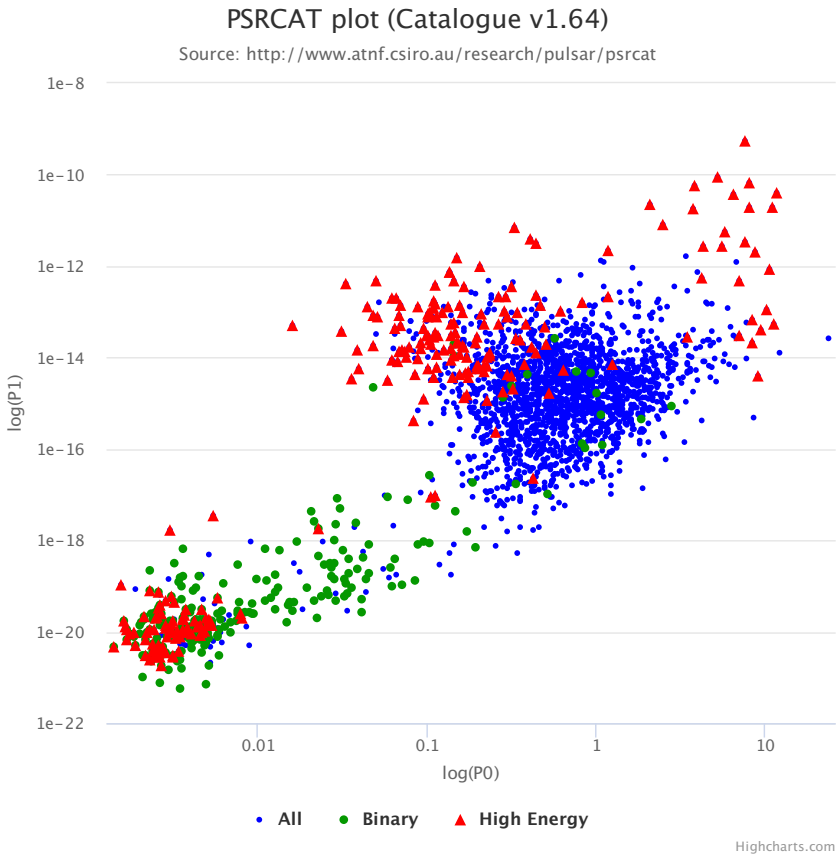

Figure 1.1: $P - \dot{P}$ diagram of all pulsars in ATNF catalog (blue small dots), including binary (green larger dots) and high energy sources (red triangles).

1.2 Pulsars: basic notions

Pulsars (PSRs) are compact objects left over from a supernova (SN) explosion. Their density is estimated to be around $\sim 10^{14}$ g cm^{-3} with a mass of $\sim 1 - 2M_{\odot}$. Thus they are compact objects, with a radius of about ~ 10 km.

PSRs are the fastest rotators known in the Universe with periods of $\sim 10^{-3} - 10$ s and have associated dipole magnetic fields of $10^8 - 10^{15}$ G, also the highest known. The period and period derivative of all pulsars known (about 3000 in the last ATNF catalog) is presented in what is called the $P\dot{P}$-diagram, depicted next.

Using the period and the period derivative of a pulsars, when such are known, we can obtain simple estimates of other relevant magntidues. For this, we use the magnetic dipole model. This model assumes that the pulsar rotates in vacuum with frequency Ω

$$\Omega = 2\pi/P, \tag{1.1}$$

and has a magnetic moment $\vec{m}$ that sustains an angle α between with the rotation axis.

The magnetic moment for a pure rotating magnetic dipole is defined (e.g., Shapiro & Teukolsky 2004)

$$|\vec{m}| = \frac{B_p R_{PSR}^3}{2}, \tag{1.2}$$

where B_p is the dipolar magnetic field and R_{PSR} is the radius of the PSR.

In this model, then, the pulsar rotational kinetic energy is transferred into magnetic and particle energy steadily, and is described by the Larmor formula

$$\dot{E} = -\frac{2}{3c^3}|\ddot{\vec{m}}|^2 \tag{1.3}$$

being c the speed of light. Substituting above,

$$\dot{E} = -\frac{B_p^2 R^6 \Omega^4 \sin^2\alpha}{6c^3}. \tag{1.4}$$

The total rotational energy of the PSR is given by

$$E = \frac{1}{2} I \Omega^2 = \frac{2\pi^2 I}{P^2}, \tag{1.5}$$

where I is the moment of inertia of the PSR (assumed as $\sim 10^{45}$ g cm^2 in the rest of this thesis). And the time derivative of the total rotational energy

$$\dot{E} = I\Omega\dot{\Omega} = -\frac{4\pi^2 I \dot{P}}{P^3} \tag{1.6}$$

Here one should note that $\dot{E} < 0$, as we have in equation (1.4), so $\dot{\Omega} < 0$, this is the so-called 'spinning-down' of the pulsar.

On the one hand, these equations allow to define the magnetic field, B_p. Its expression can be easily obtained from equations (1.4) and (1.6) giving

$$B_p = \sqrt{\frac{3Ic^3}{2\pi^2 R_{PSR}^6} P\dot{P}} \simeq 6.4 \times 10^{19} \sqrt{P\dot{P}} \text{ G}. \tag{1.7}$$

Note that sometimes the magnetic field is quoted as being a factor 2 lower ($B_e \sim 3.2 \times 10^{19}\sqrt{P\dot{P}}$). This difference depends on where we define the magnetic moment (pole or equator), since then we find this difference of a factor 2 ($B_p = 2B_e$). In general, this does not play a role in any modelling of pulsar wind nebulae, but we consistently use equation 1.7.

On the other hand, the *characteristic age* of the PSR, τ_c is defined as

$$\tau_c = -\frac{P}{2\dot{P}} = -\frac{1}{2}\left(\frac{\Omega}{\dot{\Omega}}\right)_{now} \tag{1.8}$$

where the subindex *now* means at the present time. Doing some algebra with the equations above, we obtain

$$\tau_c = \frac{3Ic^3}{B_p^2 R_{PSR}^6 \Omega_t^2 \sin^2\alpha}, \tag{1.9}$$

and using equations (1.4), (1.5) and (1.6) one can solve the rotation frequency evolution

$$\Omega(t) = \Omega_0 \left[1 + \left(\frac{\Omega_0}{\Omega_{now}}\right)^2 \frac{t}{\tau_c}\right]^{-1/2}. \tag{1.10}$$

Sometimes this is used in terms of the period,

$$P(t) = P_0 \left[1 + \left(\frac{P_{now}}{P_0}\right)^2 \frac{t}{\tau_c}\right]^{1/2}. \tag{1.11}$$

From where it is perhaps more intuitive to compute the pulsar age, setting $P(t) = P_{now}$. Thus,

$$t_{age} = \tau_c \left[1 - \left(\frac{P_0}{P_{now}}\right)^2\right]. \tag{1.12}$$

Note here that if $P_0 \ll P_{now}$, then $t_{age} \simeq \tau_c$.

The spin-down luminosity can also be written in terms of the initial period, period and period derivative

$$\dot{E} = \frac{2\pi^2 I}{\tau_c P_0^2} \left(\frac{P_{now}}{P_0}\right)^2 \left[1 + \frac{t}{\left(\frac{P_0}{P_{now}}\right)^2 \tau_c}\right]^{-2}, \tag{1.13}$$

or simply

$$\dot{E} = \dot{E}_0 \left(1 + \frac{t}{\tau_0}\right)^{-2}, \tag{1.14}$$

where τ_0 is the initial spin-down age and $\dot{E}_0$ is the initial spin-down luminosity.

We mention above that the age is not necessarily the characteristic one. This is related to the fact that $\dot{\Omega} \propto \Omega^3$ above, while this may not be (and is not) the case in general. In fact, one can define,

$$n = -\frac{P\ddot{P}}{\dot{P}}. \tag{1.15}$$

as the so-called braking index of the pulsar, and then the generalized period evolution is

$$P(t) = P_0 \left[1 + \frac{n-1}{2} \left(\frac{P_{now}}{P_0}\right)^{n-1} \frac{t}{\tau_c}\right]^{\frac{1}{n-1}}, \tag{1.16}$$

from which the age is,

$$t_{age} = \frac{2\tau_c}{n-1} \left[1 - \left(\frac{P_0}{P_{now}}\right)^{n-1}\right]. \tag{1.17}$$

and the spin-down evolution is,

$$\dot{E} = \dot{E}_0 \left(1 + \frac{t}{\tau_0}\right)^{-\frac{n+1}{n-1}}. \tag{1.18}$$

The expression for the initial spin-down power (sometimes quoted to as L_0, when the spin-down power in general is quoted as $L(t)$) is

$$\dot{E}_0 = \frac{2\pi^2 I}{\tau_c P_0^2}\left(\frac{P_{now}}{P_0}\right)^{n-1} \qquad \tau_0 = \frac{2}{n-1}\left(\frac{P_0}{P_{now}}\right)^{n-1}\tau_c. \tag{1.19}$$

Finally, τ_0 and t_{age} are related using equation (1.17),

$$\tau_0 = \frac{2\tau_c}{n-1} - t_{age}. \tag{1.20}$$

1.3 Pulsar Wind Nebulae: basic notions

Despite pulsars are best-known by, well,... their pulsations, in fact electromagnetic pulsed radiation is usually not more than just a few percent of the total energy release. Pulsars dissipate the bulk of their rotational energy via the emission of a relativistic wind of particles, or simply, the pulsar wind. From here the name: pulsar wind nebulae (PWNe) or also plerions, is derived from the ancient greek *pleres*, full (Weiler & Panagia 1978).

The wind, however, being supersonic with respect to the interstellar medium, produces a termination shock where particles can get accelerated. In a region threaded with a magnetic and photon fields, particles are able to emit at all frequencies, from radio to TeV energies. This radiation, non-thermal in nature, is what we observe as pulsar wind nebulae. In the simplest of cases, one can consider that the pulsar wind expands isotropically within the expanding shell of the supernova ejecta. Following Slane and Gelfand (2006), the position at which the wind termination shock is formed is

$$R_w = \sqrt{\frac{\dot{E}}{4\pi\chi c P_{PWN}}} \tag{1.21}$$

where $\chi = 1$ occurs when the wind is isotropic and P_{PWN} is the pressure of the gas in the PWN interior. High resolution X-ray observations have shown the ring-like emission from this termination shock, although such simplicity (see the next figure) is barely seen. Figure 1.2 shows the composite SNR–pulsar wind nebula–pulsar structure (from outer to inner layers) formed by the interstellar medium shell, the hot ejecta, reverse shock, the cold ejecta, termination shock and the central pulsar. If pulsars have a significant proper motion, or there is a significant gradient in the interstellar medium density or in other physical properties, the shapes of the PWNe can be more cigar-like, see Kargaltsev (2008, 2010) for examples.

Rather than morphology, however, this thesis focus is on the pulsar wind nebulae spectra. Nebula emission consists mostly of two components. An example of a multi wavelength spectrum of a PWN is shown in figure 1.3. On the one hand, there is synchrotron radiation coming from the particles accelerated and radiating in the magnetic

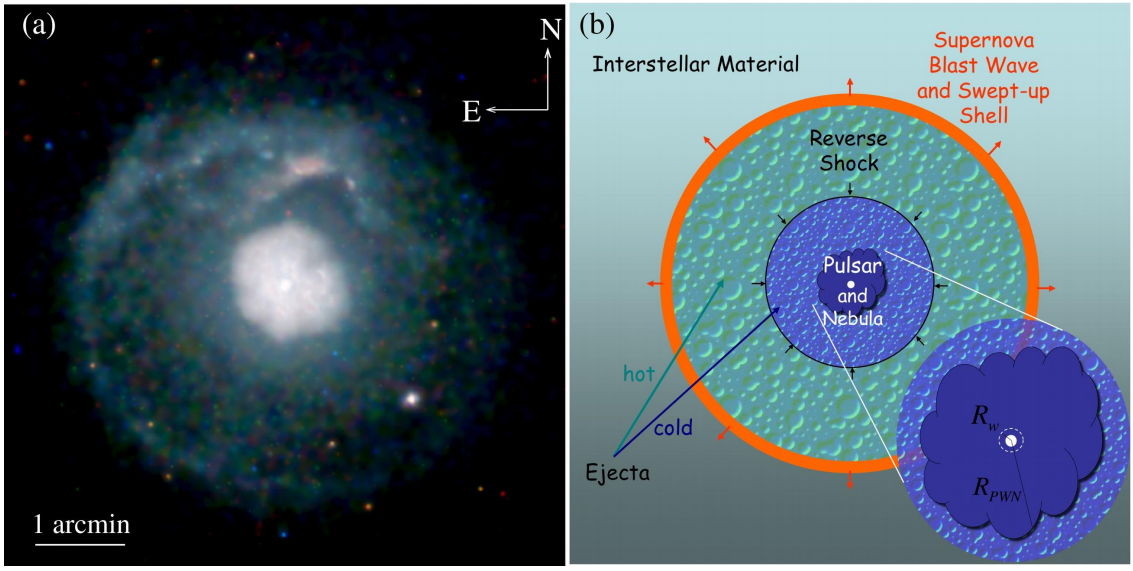

Figure 1.2: (a) A deep Chandra X-ray image of G21.5-0.9. (b) Schematic diagram of a PWN within an SNR. Figure adapted from Gaensler and Slane (2006).

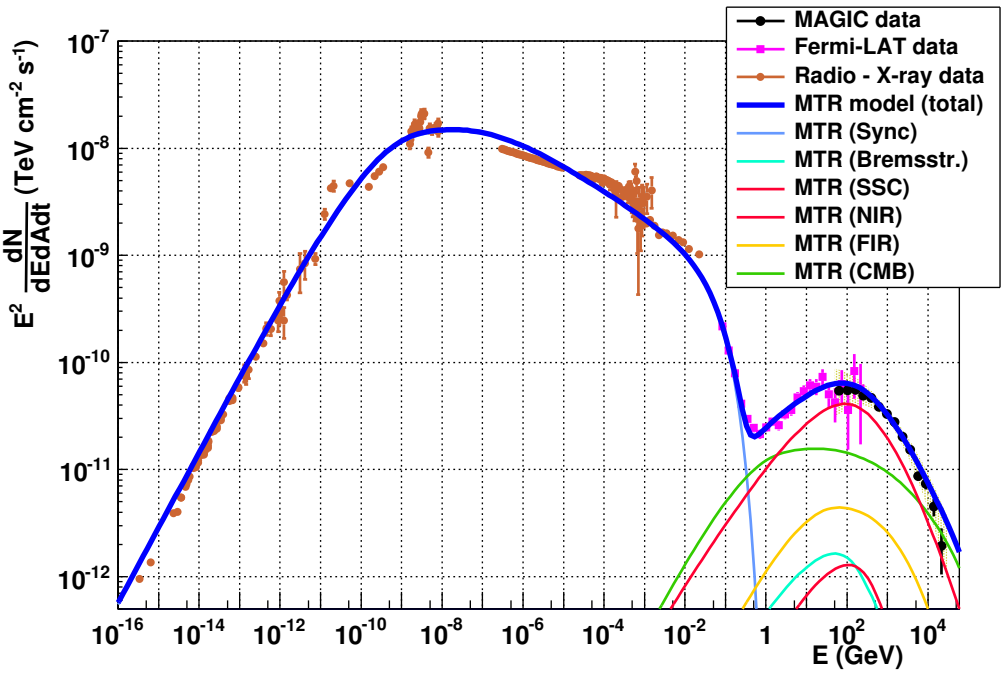

Figure 1.3: Example of a pulsar spectrum, using Crab. From radio to X-rays, the emission is well described by synchrotron emission, and from hard X-rays to VHE, the spectrum is described by the IC scattering of the electrons with the background photon fields. The model used comes from Martin, et al. 2012, and is based on earlier versions of the code TIDE as used in this thesis. The figure comes from the paper by the MAGIC collaboration (Aleksic et al. 2015)

field of the nebula. The cooling cut-off in the synchrotron spectrum is given by (e.g.., Ginzburg & Syrovatskii 1964, Ginzburg1979)

$$\nu_b = 10^{21} \left(\frac{B_{PWN}}{10^{-6}\,\mathrm{G}} \right)^{-3} \left(\frac{t}{1\,\mathrm{kyr}} \right)^{-2} \mathrm{Hz}. \tag{1.22}$$

Another useful equation of the synchrotron process relates the energy of synchrotron photons (E_{sync}) with the energy of the electrons that produce the radiation itself (E_e)

$$E_{sync} = \frac{h\nu_c}{3}, \tag{1.23}$$

where h is the Planck constant and ν_c is the so-called *synchrotron critical frequency*. The latter depends on on the magnetic field and the energy of the electrons, and explicitly, it is given by

$$\nu_c = \frac{3eB(t)E_e^2}{4\pi m_e^3 c^5}. \tag{1.24}$$

From X-rays to very high energies at TeV, instead, the radiation observed from nebulae is supposed to come from inverse Compton (IC) interaction of the high energy pairs with the low energy photons of the ambient medium, like the cosmic microwave background (CMB), the far-infrared contribution coming from the galactic ISM (FIR) and the infrared / optical contribution coming from the surrounding stars (NIR). Using the inverse Compton cross-section in the Thompson limit, the IC photons energy (E_{IC}) and the energy of the electron are related by

$$E_{IC} = \frac{4}{3} h\nu_i \left(\frac{E_e}{m_e c^2} \right)^2, \tag{1.25}$$

where ν_i is the energy of the target electrons.

The two former equations combined, plus the assumption that the CMB is the only contributor for the IC emission link the characteristic energies of the synchrotron and IC photon produced by the same electrons. And from there, one gets

$$E_{sync} \simeq 0.07 \left(\frac{E_{IC}}{1\,\mathrm{TeV}} \right) \left(\frac{B}{10\,\mu G} \right) \mathrm{keV}. \tag{1.26}$$

But care must be taken in adopting the previous field estimate. First, inverse Compton may not happen in the Thompson limit, but Klein Nishina maybe important and needs to be taken into account. Second, the assumption that CMB dominates the photon field is essentially never valid, see e.g., Tanaka et al. 2010, Torres et al. 2014 and references therein for the dominating photon field as computing from evolutionary pulsar wind nebulae models, where it is shown that IR is in fact most usually dominating. Note that electrons required to emit in X-rays for reasonable values of magnetic fields are more energetic than those necessary to emit in TeV by inverse Compton When the magnetic field goes down with the pulsar aging, the synchrotron flux decreases and the inverse Compton component increases since when electrons lose energy, the population of pairs

able to reach to TeV energies increases. This kind of simple analysis explains both, the relative sizes of PWN at both X-rays (more compact) and gamma-rays (more diffuse), as well as why we have detected so many middle-aged PWNe in γ-rays that have not been detected at lower wavelengths.

1.4 Modelling PWN using the code TIDE: basic notions

In the basis of our research is the modelling of the time-dependent evolution of the pulsar wind nebulae, together with its radiation, using the code TIDE (see e.g., Martin et al. 2012; 2016). This model computes the evolution in time of the pair distribution within the PWN under synchrotron, inverse Compton, and Bremsstrahlung interactions, adiabatic losses, and accounting for escaping particles. i.e., it solves

$$\frac{\partial N(\gamma,t)}{\partial t} = Q(\gamma,t) - \frac{\partial}{\partial \gamma}\left[\dot{\gamma}(\gamma,t)N(\gamma,t)\right] - \frac{N(\gamma,t)}{\tau(\gamma,t)}. \tag{1.27}$$

The second term on the right hand side takes into account the energy losses due to synchrotron, inverse Compton, and Bremsstrahlung interactions, as well as the adiabatic losses. The last term on the right hand side accounts for escaping particles (we assume Bohm diffusion). Expressions for the radiative losses (inputed in the code devoid of any simplifications) can be found in Martin, et al. (2012). Time dependences included are the spin-down power, the particle injection, and their losses. The magnetic field also varies in time as a result of the balance between the instantaneous injection (the fraction of spin-down that goes to power the magnetic field, η, which is assumed constant in time) and the adiabatic losses of the field due to the expansion of the PWN. η is also usually called the magnetic fraction of the nebula. The radiative losses of the particle population are taken into account also when determining the inner pressure of the nebula. The injection function for pairs is assumed as a broken power law. That is,

$$Q(\gamma,t) = Q_0(t) \begin{cases} \left(\frac{\gamma}{\gamma_b}\right)^{-\alpha_1} & \text{for} \quad \gamma \leq \gamma_b, \\ \left(\frac{\gamma}{\gamma_b}\right)^{-\alpha_2} & \text{for} \quad \gamma > \gamma_b, \end{cases} \tag{1.28}$$

where the normalization term $Q_0(t)$ is computed using the spin-down luminosity of the pulsar $\dot{E}(t)$, later to be referred as $L_{sd}(t)$

$$(1-\eta)\dot{E}(t) = \int_{\gamma_{min}}^{\gamma_{max}} \gamma m_e c^2 Q(\gamma,t) \mathrm{d}\gamma, \tag{1.29}$$

No other source of energy is considered.

The maximum energy that can be achieved is determined either by the synchrotron limit, established by the balance between the energy loss by particles due to synchrotron radiation and the energy gain during acceleration,

$$\gamma_{max}^{sync}(t) = \frac{3 m_e c^2}{4e}\sqrt{\frac{\pi}{eB(t)}}, \tag{1.30}$$

where e is the electron charge and B the mean magnetic field of the PWN, or by demanding confinement of the particles inside the termination shock of the PWN where particles are accelerated. The latter implies

$$\gamma_{max}^{gyro}(t) = \frac{\epsilon e \kappa}{m_e c^2}\sqrt{\frac{\eta L(t)}{c}}, \tag{1.31}$$

being κ the magnetic compression ratio (we fix it as 3) and ϵ is the containment fraction ($\epsilon < 1$). This is also the reason why a change in confinement factor affects the electron population, and ultimately the SED. The code takes the stringent of these limits.

The radius of the PWN is computed taken into account reverberation processes when they happen, according to age, progenitor explosion, medium density, and pressure. After reverberation, a Sedov expansion is activated when the PWN pressure reaches that of the SNR's Sedov solution.

For the magnetic field evolution, the code assumes:

$$\frac{dW_B(t)}{dt} = \eta L_{sd}(t) - \frac{W_B(t)}{R(t)}\frac{dR(t)}{dt}, \tag{1.32}$$

where $W_B = B^2 R^3/6$ the total magnetic energy, and from where results

$$B(t) = \frac{1}{R^2(t)}\sqrt{6\eta \int_0^t L_{sd}(t')R(t')\mathrm{d}t'} \tag{1.33}$$

whereas for the dynamical evolution the code solves the array of equations:

$$\frac{dR(t)}{dt} = v(t), \tag{1.34}$$

$$M(t)\frac{dv(t)}{dt} = 4\pi R^2(t)\left[P(t) - P_{ej}(R,t)\right], \tag{1.35}$$

$$\frac{dM(t)}{dt} = 4\pi R^2(t)\rho_{ej}(R,t)(v(t) - v_{ej}(R,t)). \tag{1.36}$$

Eq. (4.11) only applies if $v_{ej}(R,t) < v(t)$. Otherwise, $dM(t)/dt = 0$. To compute the pressure of the nebula the model considers both the field and the particles, such that

$$P(t) = P_p(t) + P_B(t), \tag{1.37}$$

and where

$$P_B(t) = \frac{B^2(t)}{8\pi}, \tag{1.38}$$

and the pressure contributed by particles is

$$P_p(t) = \frac{3(\gamma_{pwn} - 1)E_p(t)}{4\pi R(t)^3}. \tag{1.39}$$

The energy of particles is computed directly from the total population (i.e., it consider radiative losses)

$$E_p(t) = \int_{\gamma_{min}}^{\gamma_{max}} \gamma m_e c^2 N(\gamma, t)\mathrm{d}\gamma. \tag{1.40}$$

The PWN bounces and starts the Sedov phase when its pressure reaches the pressure of the SNR's Sedov solution, and from there onwards it evolves following this equation

$$R^4(t_{Sedov})P(t_{Sedov}) = R^4(t)P(t). \tag{1.41}$$

Changes or further details related to the formulae above are given when we use the code in the next chapters.

Chapter 2

The pulsar wind nebula complex PSR J0205+6449/3C 58

Contents of this chapter

I present here the results of the analysis of 8 years of *Fermi*-LAT data of the pulsar/pulsar wind nebula complex PSR J0205+6449/3C 58. These results were first published, together with my coauthors, in Li et al. 2018, The Astrophysical Journal, Volume 858, Issue 2, article id. 84, 7 pp. (2018). I was particularly responsible for establishing the pulsar wind nebulae modelling of the data, and participated in the writing and discussion of the rest of the work in which the chapter is based. This work was an official *Fermi*-LAT paper, that implies it was internally refereed previously to being externally refereed as well at the journal.

Using a contemporaneous ephemeris, we here present a detailed analysis of PSR J0205+6449 both during its off-peak and on-peak phase intervals. 3C 58 is significantly detected during the off-peak phase interval. We show that the spectral energy distribution at high energies is the same disregarding the phases considered, and thus that this part of the spectrum is most likely dominated by the nebula radiation. We present results of theoretical models of the nebula and the magnetospheric emission that confirm this interpretation. Possible high-energy flares from 3C 58 were searched for, but none was unambiguously identified.

2.1 Introduction

3C 58 is an extended flat-spectrum radio source which was identified as a supernova remnant (SNR) first in radio (Weiler & Seielstad 1971) and then in optical by Hα observations (van den Bergh 1978). Because of its flat radio spectrum and bright-filled center, 3C 58 was classified as a pulsar wind nebula (PWN, or plerion, Weiler & Panagia

1978) long before the central pulsar, PSR J0205+6449, was discovered (Murray et al. 2002). Subsequent radio imaging observations continued to reveal a center-brightened morphology and a compact size of 6'×9' (Green 1986; Reynolds & Aller 1988; Bietenholz et al. 2001, 2006), which is consistent with the morphology observed in infrared and X-ray bands (Bocchino et al. 2001; Slane et al. 2004, 2008). Since the jet-torus structure (Slane et al. 2004), filaments and knots (Fesen et al. 2008) observed in 3C 58 resemble those seen in the Crab Nebula, 3C 58 was proposed to be a "Crab-like" PWN. The distance of 3C 58 was estimated as 3.2 kpc (Roberts et al. 1993), although there is an on-going discussion on this value, given that a recent H I measurement suggests a nearer distance of just 2 kpc (Kothes 2013). 3C 58 was proposed to be the remnant of SN 1181, observed by Chinese and Japanese astronomers (Stephenson 1971; Stephenson & Green 2002). However, there is controversy on the viability of this connection (see Fesen et al. 2008, Table 3 and Kothes 2013, Table 1 for a discussion).

PSR J0205+6449 is a pulsar with a rotational period of 65 ms located in 3C 58. It was discovered by *Chandra* in X-rays many years after 3C 58 was classified as a PWN. Timing parameters give a surface magnetic field estimation of 3.6×10^{12} G, a characteristic age of 5400 yr, and a very high spin-down luminosity, 2.7×10^{37} erg s^{-1}, making it the third most energetic of the known Galactic pulsars (Murray et al. 2002). Camilo et al. (2002) reported the detection of its radio pulsation, which leads the X-ray pulse by ~ 0.10 spin phase. Because of the high spin-down power of PSR J0205+6449, it was expected to shine in gamma rays. PSR J0205+6449 was among the first gamma-ray pulsars detected by *Fermi*-LAT (Abdo et al. 2009). Gamma-ray emission from the PWN 3C 58 was reported in the second *Fermi*-LAT Pulsar Catalog (Abdo et al. 2013, which we shall refer to as 2PC hereafter). 3C 58 was also detected above 10 GeV in the First and Third Catalog of Hard *Fermi*-LAT Sources, suggesting its potential nature as a TeV gamma-ray source (Ackermann et al. 2013, 1FHL; Ajello et al. 2017, 3FHL). Several imaging atmospheric Cherenkov telescopes have observed 3C 58 (*Whipple*, Hall et al. 2001; VERITAS, Aliu 2008; MAGIC I, Anderhub et al. 2010) but it was only recently detected by MAGIC II (Aleksić et al. 2014). PWN models for 3C 58 have been presented by Bednarek & Bartosik (2003, 2005), Bucciantini et al. (2011), and Torres et al. (2013); in the latter paper, a comparison among these models is provided. Here, in an effort to understand better the radiation from the complex, we report on further analysis/modeling of PSR J0205+6449/3C 58 using more than eight years of *Fermi*-LAT data and the newest response functions.

2.2 Observations

The *Fermi*-LAT (Atwood et al. 2009) data used here range from 2008 August 4 (MJD 54682) to 2016 September 20 (MJD 57651), covering 97 months and extending the three years' coverage of the 2PC. *Fermi* Science Tools[1], 10-00-05 release was used to analyze the data. The data selection and analysis method adopted here are similar with those in Li et al. 2017, i.e., We selected events from the "Pass 8" event class, and used "P8R2 V6 Source" instrument response functions (IRFs). All gamma-ray photons within an energy range of 0.1–300 GeV and a circular region of interest (ROI) of 10° radius centered on PSR J0205+6449 were considered. Gamma-ray photons were selected only with a zenith angle $< 90°$ to reject contaminating gamma rays from the Earth's limb.

The spectral results presented in this work were calculated by performing a binned maximum likelihood fit (30 logarithmically spaced bins in the 0.1–300 GeV range) using the Science Tool *gtlike*. A spectral-spatial model was constructed including Galactic and isotropic diffuse emission components ("gll_iem_v06.fits", Acero et al. 2016, and "iso_P8R2_CLEAN_V6_v06.txt", respectively[2]) as well as known gamma-ray sources within 15° of the 3C 58, based on *Fermi* LAT Third Source Catalog (3FGL, Acero et al. 2015). The spectral parameters of the sources within 3° of our target were left free. The spectral parameters of other sources included were fixed at the 3FGL values. In the pulsar phase-resolved analysis, photons within a specific spin phase interval are selected. To account for that, the prefactor parameters of all sources were scaled to the width of the spin phase interval. The significance of the sources are evaluated by the Test Statistic (TS). This statistic is defined as $\mathrm{TS}=-2\ln(L_{max,0}/L_{max,1})$, where $L_{max,0}$ is the maximum likelihood value for a model in which the source studied is removed (the "null hypothesis"), and $L_{max,1}$ is the corresponding maximum likelihood value with this source incorporated. The larger the value of TS, the less likely the null hypothesis is correct (i.e., a significant gamma-ray excess lies on the tested position). The square root of the TS is approximately equal to the detection significance of a given source. The *pointlike* analysis package (Kerr 2011a) was used to produce the TS maps. In the analysis, the systematic errors have been estimated by repeating the analysis using modified IRFs that bracket the effective area[3] (Ackermann et al. 2012), and artificially changing the normalization of the Galactic diffuse model by ± 6% (2PC). The latter dominates the systematic errors. Energy dispersion correction has been adopted in spectral analysis[4]. The first (second) uncertainty shown corresponds to the statistical (systematic) error.

To search for the possible spatial extension of 3C 58 in the off-peak gamma-ray

[1] *http://fermi.gsfc.nasa.gov/ssc/*
[2] *http://fermi.gsfc.nasa.gov/ssc/data/access/lat/BackgroundModels.html*
[3] *http://fermi.gsfc.nasa.gov/ssc/data/analysis/scitools/Aeff_Systematics.html*
[4] *https://fermi.gsfc.nasa.gov/ssc/data/analysis/documentation/Pass8_edisp_usage.html*

emission, we followed the method described in Lande et al. (2012). The source is modeled to be spatially extended with a symmetric disk model. We fitted its position and extension with the *pointlike* analysis package. The extension significance was defined as $\mathrm{TS}_{ext}=-2(\ln L_{point}/L_{disk})$, in which L_{disk} and L_{point} were the *gtlike* global likelihood of the extended source hypotheses and the point source, respectively. A threshold for claiming the source to be spatially extended is set as $\mathrm{TS}_{ext}>16$, which corresponds to a significance of $\sim 4\sigma$.

2.3 Off-peak and on-peak phase selection

Photons from PSR J0205+6449 within a radius of 0.65^0 and a minimum energy of 200 MeV were selected, which maximized the H-test statistic (de Jager et al. 1989; de Jager & Büsching 2010). Adopting the most updated ephemeris for PSR J0205+6449 (M. Kerr & D. Smith 2017, private communication), we assigned pulsar rotational phases to each gamma-ray photon that passed the selection criteria, using *Tempo2* (Hobbs et al. 2006) with the *Fermi* plug-in (Ray et al. 2011).

The light curve of PSR J0205+6449 was divided into two parts, an off-peak and an on-peak interval. We began by deconstructing the pulsed light curve into simple Bayesian Blocks using the same algorithm described in the 2PC, by Jackson et al. (2005) and Scargle et al. (2013). To produce Bayesian Blocks on the light curve, we have extended the data over three rotations, by copying and shifting the observed phases to cover the phase range from -1 to 2. We have defined the final blocks to be between phases 0 and 1. To increase the statistics and in accordance with the current results, we have adopted a wider interval for the off-peak phases than that used in the 2PC (0.35 of the total). The off-peak interval in our analysis is then defined to be at ϕ=0.0−0.184, 0.291−0.574 and 0.786−1.0, yielding 0.681 of the the total revolution. We also tested a conservative selection for the off-peak phases, selecting them as ϕ=0.0−0.144 and 0.825−1.0, which is defined as the lowest Bayesian block with 10% reduction on either side (2PC), yielding 0.319 of the total revolution. It leads to consistent results. The on-peak phases are thus located at ϕ=0.184−0.291 and ϕ=0.574−0.786. Figure 2.1 shows the pulsar spin light curves, using a photon weighting technique based on the method of Kerr (2011b). Additional discussion of Figure 2.1 is presented in Section 2.5.

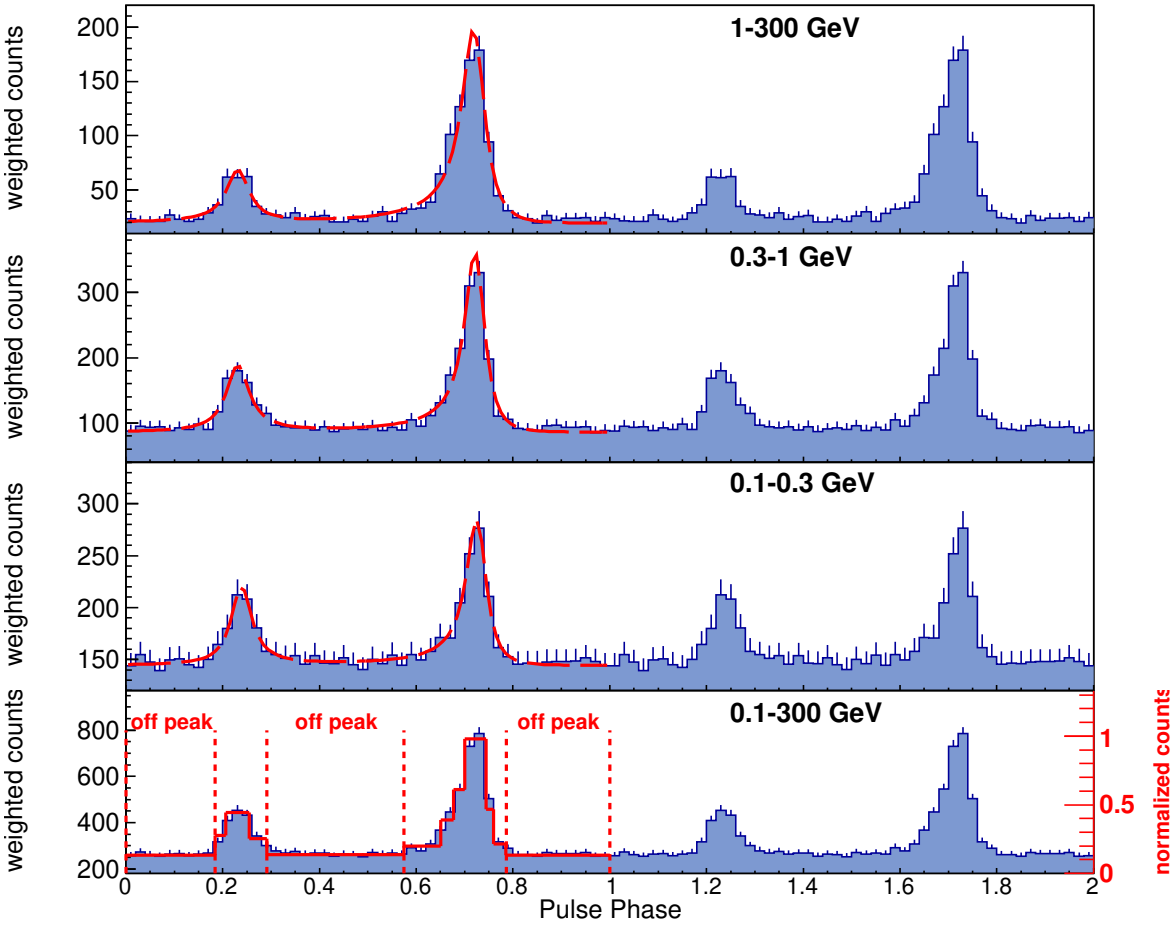

Figure 2.1: Weighted pulse profile of PSR J0205+6449 at different energies. Two rotational pulse periods are shown, with a resolution of 50 phase bins per period. The double asymmetric Lorentzian profiles plus a constant that we have fitted to the light curves are shown with dashed red lines. The bottom panel shows the weighted pulse profile above 100 MeV. The Bayesian block decomposition is represented by red lines in the bottom panel, and is normalized to the highest block. The red dotted lines define the off-peak intervals.

2.4 Off-peak analysis: detecting the gamma-ray emission from PWN 3C 58

The off-peak emission of PSR J0205+6449/3C 58 was previously reported in the 2PC using three years of data with P7V6 IRFs (P7V6 is one of the previous versions of LAT IRFs[5]), yielding a TS value of 33.7 and a flux level of (1.75 ± 0.68) × 10^{-11} erg $cm^{-2}s^{-1}$ in the 0.1–316 GeV range. This emission was thought to be the pulsar wind nebula radiation. 3FGL was based on four years of Pass 7 LAT data while in this analysis the dataset is doubled (eight years Pass 8 data). Thus the region around PSR J0205+6449/3C 58 may not be well modelled solely by 3FGL sources. For a better spectral-spatial modelling of this region, we added three additional point sources (assumed to be described by a simple power law) to the spatial model (Figure 2.2), using a similar method as Caliandro et al. (2013). The best positions of the additional sources were determined with *pointlike* as R.A. = $31^0$19±0.05, decl.= $66^0$91±0.04 (NEW 1); R.A. = $33^0$59±0.05, decl.= $62^0$52±0.04 (NEW 2); R.A. = $35^0$30±0.04, decl.= $62^0$92±0.04 (NEW 3). Assuming a power law spectral shape ($dN/dE = N_0(E/E_0)^{-\Gamma}$ cm^{-2} s^{-1} GeV^{-1}), the off-peak analysis of PSR J0205+6449/3C 58 results in a TS value of 202 and a flux level of (1.24 ± 0.13 ± 0.17) × 10^{-11} erg $cm^{-2}s^{-1}$ in the 0.1–300 GeV energy range, which is consistent with 2PC results. The spectral index is estimated as 2.04 ± 0.07 ± 0.15 (Table 2.1), which is softer than the value reported in the 2PC (1.61±0.21) but still within 3 σ errors. Figure 2.2, left panel shows the TS map of PSR J0205+6449/3C 58 region during off-peak phases. In off-peak phases we also modeled PSR J0205+6449/3C 58 with a power law having an exponential cutoff ($dN/dE = N_0(E/E_0)^{-\Gamma}\exp(-E/E_0)$ cm^{-2} s^{-1} GeV^{-1}). The two models are compared using the likelihood ratio test (Mattox et al. 1996). The ΔTS is defined as $\Delta TS = -2\ln(L_{PL}/L_{CPL})$, where L_{CPL} and L_{PL} are the maximum likelihood values for power-law models with and without a cut off. The ΔTS between the two models is 0.03, which indicates that a cutoff is not significantly preferred. This result is also consistent with the 2PC. The best-fit spectral parameters and corresponding TS values are listed in Table 2.1, while the spectral energy distributions (SEDs) along with the best-fit power law model are shown in Figure 2.3, left panel. The SEDs are produced by repeating the likelihood analysis in 12 equally spaced logarithmic energy bins, with photon index fixed at 2.04.

The extension of PSR J0205+6449/3C 58 during off-peak phases was explored as well in the 2PC analysis, but has not been favored over a point-like morphology. Here, using *pointlike*, we have fitted an extended disk to the off-peak gamma-ray emission of PSR J0205+6449/3C 58, yielding a $\Delta TS_{ext} = 0.1$; the disk is not favored either. The localization of the off-peak emission determined with *pointlike* is R.A. = $31^0$40,

[5] *http://fermi.gsfc.nasa.gov/ssc/data/analysis/documentation/Cicerone/Cicerone_LAT_IRFs/IRF_overview.html*

Table 2.1: *Fermi*-LAT spectral parameters of PSR J0205+6449 during off-peak and on-peak phases. The first (second) uncertainties correspond to statistical (systematic) errors.

Phase Interval	Spectral Index	Cutoff Energy (GeV)	TS	Flux, 0.1–300 GeV 10^{-11} erg cm^{-2}s^{-1}
phase averaged	2.06 ± 0.04 ± 0.14	5.05 ± 0.07 ± 1.22	4213	5.53 ± 0.13 ± 0.46
off-peak	2.04 ± 0.07 ± 0.15	-	202	1.24 ± 0.13 ± 0.17
on-peak	1.93 ± 0.04 ± 0.08	2.87 ± 0.03 ± 0.46	7718	15.31 ± 0.27 ± 0.88

decl.= $64^0$83, with a 95% confidence error circle of radius $0^0$025, which is consistent with PSR J0205+6449/3C 58. Considering the flat spectrum and the absence of a spectral cutoff, it is natural to propose that the off-peak gamma-ray emission of PSR J0205+6449/3C 58 is dominated by the PWN 3C 58, though a weak magnetospheric component cannot be completely ruled out at low energies. 3C 58 was also detected in the 1FHL and the 3FHL catalogs, and the reported spectra are consistent with our results. The detected morphology of 3C 58 being point-like in 0.1–300 GeV is not unexpected. The arcmin-sized extension in radio and X-rays (Bietenholz et al. 2001; Bocchino et al. 2001) is smaller than the *Fermi*-LAT PSF (e.g. 0.1 at 10 GeV).

2.5 On-peak analysis: magnetospheric emission

We have considered a power law with an exponential cutoff for modeling the on-peak emission of PSR J0205+6449. The best-fit parameters are shown in Table 2.1. The right panel of Figure 2.2 shows the on-peak TS map of the PSR J0205+6449 region. Its SED is shown in Figure 2.3. At high energies, the SED is consistent with that derived for the off-peak, which indicates that the PWN 3C 58 dominates the flux. Alternative spectral shapes, like a power law with a sub-exponential cutoff ($dN/dE = N_0(E/E_0)^{-\Gamma}\exp(-E/E_0)^b$ cm^{-2} s^{-1} GeV^{-1}, leaving the exponential index b free) yield a ΔTS= 5 and are thus not preferred.

We have also modeled the phase-averaged emission of PSR J0205+6449 with a power law having an exponential cutoff. The best-fit parameters are shown in Table 2.1 and the

SED is shown in Figure 2.3, right panel. Adopting the best-fit spectral model derived, we calculated the probabilities for photons to come from PSR J0205+6449 within a radius of 3°, using the tool *gtsrcprob*, and produced a weighted pulsed light curve based on these photons (Kerr 2011b). The bottom panel of Figure 2.1 shows the folded, pulsed light curve above 100 MeV. The remaining panels of the same figure show the light curve in narrower energy bands. The light curve shows two distinct peaks, which is consistent with the profile reported by Abdo et al. (2009) and the 2PC. To locate the two peaks, we fitted the light curve with two asymmetric Lorentzian functions plus a constant (Figure 2.1). The fitted constant accounts for the background, which as we have just shown, is dominated by the PWN 3C 58. The first (P1) and second (P2) peaks are at 0.234±0.003 and 0.719±0.001, respectively. The separation between the two peaks is 0.485±0.003, which is consistent with Abdo et al. (2009). The phase reference used is different from Abdo et al. (2009). By shifting ~ 0.149 spin phase, P2 would be aligned with the profile in Abdo et al. (2009). In that case, the gamma-ray profile we observed is in good alignment with the X-ray profile but is offset from the radio pulse by ~ 0.085.

The strength of P1 and P2 is calculated as the sum of the weighted counts during corresponding on-peak phase (ϕ_1=0.184−0.291 and ϕ_2=0.574−0.786, respectively) minus the background. The relative strength of P1 and P2 decreases significantly from low to high energies (Figure 2.4, left panel), as first reported by Abdo et al. (2009). A similar trend was observed in Vela, Crab, Geminga, B1951+32, and J0007+7303 pulsars (Thompson 2001; Kanbach 1999; Aleksić et al. 2014b; Li et al. 2016), which shows a spectral energy dependence of the gamma-ray light curve. We carried out spectral analysis for the two peaks. In the corresponding on-peak phase for the two peaks (ϕ_1=0.184−0.291 and ϕ_2=0.574−0.786), the pulsar spectrum is modeled as a power law with an exponential cutoff. The right panel of Figure 2.4 shows the spectral parameters of PSR J0205+6449 in the two on-peak phases. The lower cut-off energy of P1 when compared with that obtained for P2 (Figure 2.4, right panel) explains the energy evolution of the P1/P2 ratio.

In order to search for Crab-like flares (Abdo et al. 2013; Buehler et al. 2012) from 3C 58, we produced light curves with a 30-days time bin in the 0.1–1 GeV and 1–10 GeV bands during the off-peak phase and in 10–300 GeV during all spin phases. The spectral index is fixed at the best-fit value along the off-peak phases, as listed in Table 2.1. All the light curve data points are below the detection threshold of TS=25; therefore we find no evidence of flaring on this time scale.

2.6 Summary and discussion

Using 8.5 years of *Fermi*-LAT data and a contemporaneous ephemeris, we carried out a detailed analysis of PSR J0205+6449 both during its off-peak and on-peak phase intervals.

During the off-peak phases, PSR J0205+6449/3C 58 is significantly detected, having a TS value of 202. Its spectrum can be modeled by a simple power law. No extension is detected. The flat spectrum and the non-detection of a spectral cutoff argue for a PWN origin of the off-peak gamma-ray emission of PSR J0205+6449/3C 58. The top panel of Figure 2.5 shows a theoretical model of the nebula, based on a time-dependent integration of the dynamical evolution of both the nebula and the supernova remnant, the radiation of particles, and the particle population. For details on the model see Martin et al. (2016) and the appendix in Torres (2017). The spin-down power, the particle injection, the energy losses, and the magnetic field all depend on time, and their dependence are accounted for in the model. The particle content of the nebula is obtained from the balance of energy losses, injection, and escape. We include losses by synchrotron, inverse-Compton (Klein Nishina inverse Compton with the cosmic-microwave background as well as with IR/optical photon fields), self-synchrotron Compton, and bremsstrahlung, devoid of any radiative approximations, and compute the radiation produced by each process. The model also considers the dynamical influence of the reverse shock travelling backwards towards the pulsar, and compressing the nebula. However, given that the pulsar is young, this effect is not found to be relevant and results would be very similar if neglected altogether: the nebula is freely expanding. We find a good agreement with data considering a nebula at 3.2 kpc (the same distance we use below for the computation of the pulsar magnetospheric power) and an age of 2500 years. The fitting model features a broken power law for injected electrons at the termination shock, with a low (high) energy index of 1.1 and 2.94, and an energy break at Lorentz factor 9×10^4. These values of the parameters (as well as the magnetic energy fraction) are in agreement with our earlier analysis (Torres, Cillis, & Martin 2013). The magnetic fraction (the fraction of spin-down energy that goes into the magnetic field) is 0.2; thus 3C 58 is a particle-dominated nebula; Nevertheless the magnetic field has one of the highest energy reservoirs when compared with all other nebulae of similar age, perhaps with exception of CTA 1 (see Torres et al. 2014). Using the current data, we have seen that there is a degeneracy regarding which inverse Compton contribution dominates at high energies. We have explored about a thousand models varying the energy densities and temperatures for the NIR and FIR photon backgrounds and the best fitting one has similar contributions of both. Thus, we can find models where one or the other dominates without changing the overall fit significantly (e.g., within a factor of 1.3 of the miminum χ^2). Further data would be needed to distinguish among these possibilities; in particular, 3C 58 will be a bright source for the Cerenkov Telescope Array. Observations with this facility will help determine

the peak and the fall-off of the gamma-ray emission, distinguishing between NIR- or FIR-dominated scenarios.

For the on-peak interval, PSR J0205+6449 can be modeled by a power law with an exponential cutoff. We explored the existence of a sub-exponential cutoff, but no improvement was found. PSR J0205+6449 shows a two-peak pulse profile. The ratio of P1 and P2 decreases significantly with energy (Figure 2.4, left panel). This is consistent with the cut-off energy of P1 being lower than that obtained for P2 (Figure 2.4, left panel).

The most common interpretation of the magnetospheric radiation for this and all other gamma-ray pulsars is that it originates in synchro-curvature radiation in a high-altitude gap (alternatively see, e.g., Cerutti et al. 2015). To consider further this statement we have applied the model discussed in detail in Vigano & Torres (2015) and Vigano, Torres, & Martin (2015). In this model, the detectable radiation coming from the magnetosphere can be estimated by integrating the single-particle synchro-curvature spectrum along the travelled distance in the gap, convolved with an effective particle distribution, dN/dx, where x is the distance along the magnetic field line (see Vigano et al. 2015 for more details on the computation of the synchro-curvature power):

$$\frac{dP_{\rm gap}}{dE_\gamma} = \int_{x_{\rm in}}^{x_{\rm out}} \frac{dP_{\rm sc}}{dE_\gamma}\frac{dN}{dx}{\rm d}x \ . \qquad \text{with} \qquad \frac{dN}{dx} = N_0 \frac{e^{-(x-x_{\rm in})/x_0}}{x_0(1-e^{-x_{\rm out}/x_0})} \ . \tag{2.1}$$

The effective particle distribution represents the number of particles, per unit of distance, emitting radiation towards us. In this model, two parameters, the electric field $E_{||}$ accelerating particles, and the degree of uniformity of the particle's distribution along the trajectory, $x_0/R_{\rm lc}$, define the spectrum completely. On the contrary, the normalization N_0 moves the spectrum up and down in luminosity, without modifying its shape. We have applied this model to the phase-averaged SED (i.e., *Fermi*-LAT data only and a fixed magnetic gradient $b = 2.5$, as in Vigano, Torres, & Martin 2015) and find a good match for the values shown in Figure 2.5, bottom panel. The fitting results are consistent with those in Vigano et al. 2015. Our current analysis gives $\log N_0 = 30.90^{+0.21}_{-0.30}$ compared to the value of $\log N_0 = 29.93^{+0.67}_{-0.33}$ in Vigano et al. 2015. Whereas applying the model to the on-peak phase spectrum only would lead to comparable results (given that the spectral index of both the phase averaged and on-peak spectra are the same within errors, and the cutoff energy is only slightly different), the phase-averaged fit allows a comparison with other gamma-ray pulsars for which only averaged spectral results are currently available. PSR J0205+6449's fit parameters (that result well in agreement with those found using earlier data – see Table 2 of Vigano, Torres, & Martin 2015) confirm the reported trend relating $E_{||}$ to $x_0/R_{\rm lc}$ (see the first panels in Figure 2 of Vigano, Torres, & Martin 2015), emphasizing that synchro-curvature dominated radiation is likely behind the pulsations. We note that PSR J0205+6449 is part of the soft gamma-ray pulsar catalog and it has

also been detected in X-rays (Kuiper & Hermsen 2015). For a complete model of the pulsed spectrum considering also the X-ray data, and further discussion, see Torres et al. 2018.

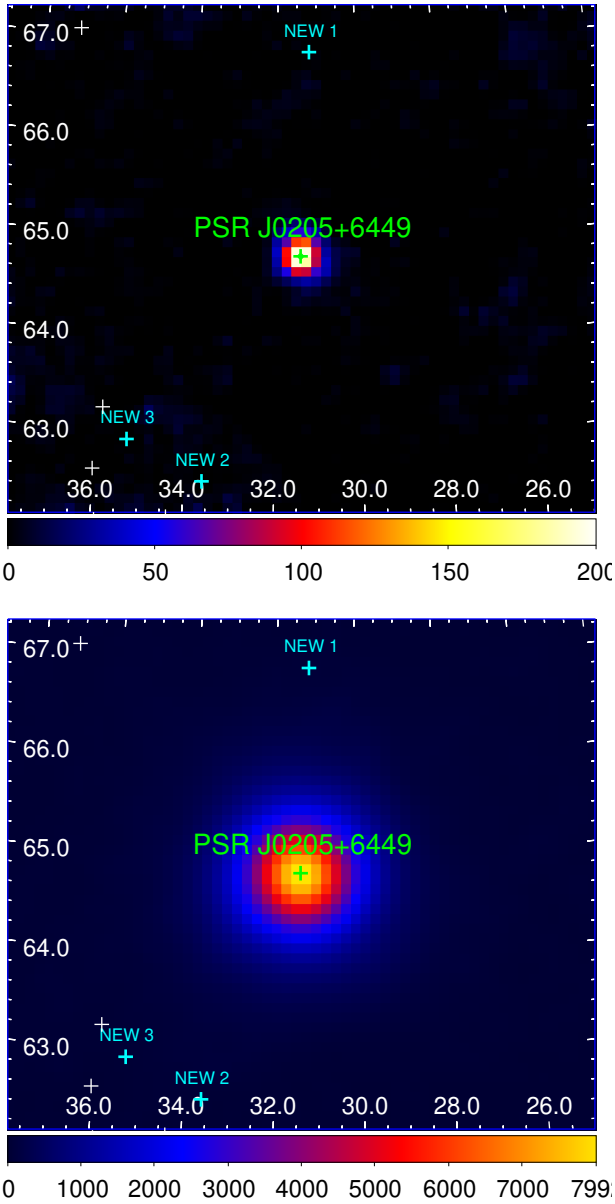

Figure 2.2: TS map (0.1–300 GeV) of the *Fermi*-LAT field surrounding PSR J0205+6449 during off-peak (left) and on-peak (right) phases. The position of PSR J0205+6449 is shown as a green cross while other sources included in the model from 3FGL are shown as white crosses. The new sources added in the analysis are shown with cyan crosses. The X-and Y-axis are R.A. and decl. referenced at J2000.

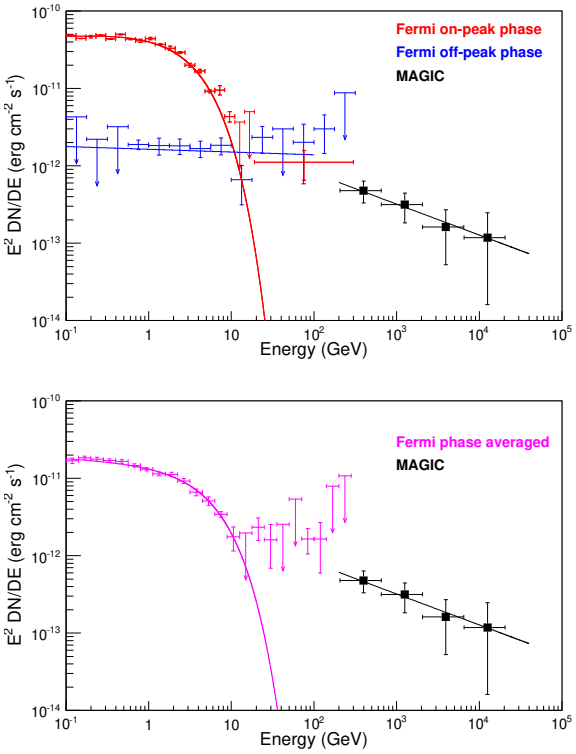

Figure 2.3: Left: *Fermi*-LAT spectra of PSR J0205+64493C 58 during off-peak (blue) and on-peak (red) phases. A 95% upper limit is calculated if the TS of the SED point is less than 9. Maximum likelihood models fitted with *gtlike* are shown with red lines (power law with exponential cutoff) and blue lines (power law). The MAGIC spectral points and overall fit (Aleksić et al. 2014a) are shown in black for comparison. Right: phase-averaged (purple) *Fermi*-LAT spectrum of PSR J0205+6449 shown with the maximum likelihood model fitted with *gtlike* (a power law with exponential cutoff). The errors shown here are statistical.

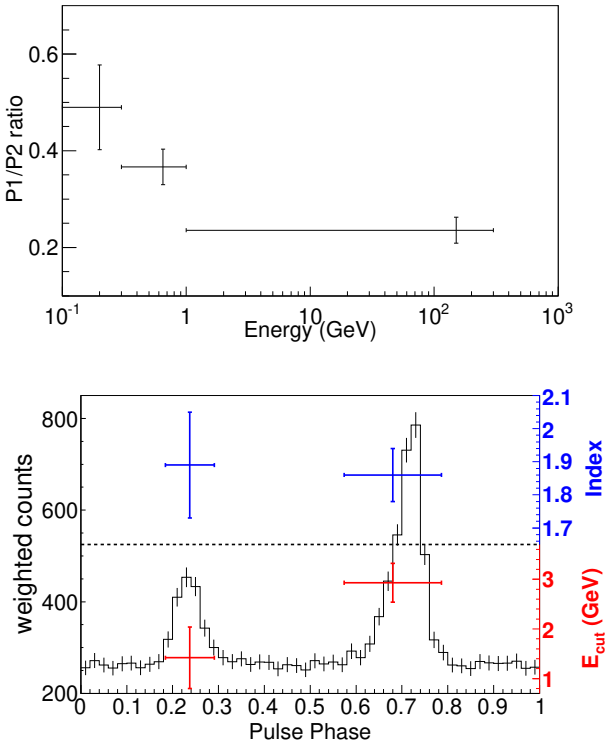

Figure 2.4: Left: Energy evolution of the P1/P2 ratio. The energy bins are the same as in Figure 2.1. Right: Spectral parameters of PSR J0205+6449 during the two on-peak intervals. The histogram shows the weighted phaseogram of PSR J0205+6449 for energies between 0.1 and 300 GeV (similar to Figure 2.1, bottom panel). The red and blue points correspond to the cutoff energy and the spectral index of the power law with exponential cutoff model, respectively. Systematic errors have also been considered.

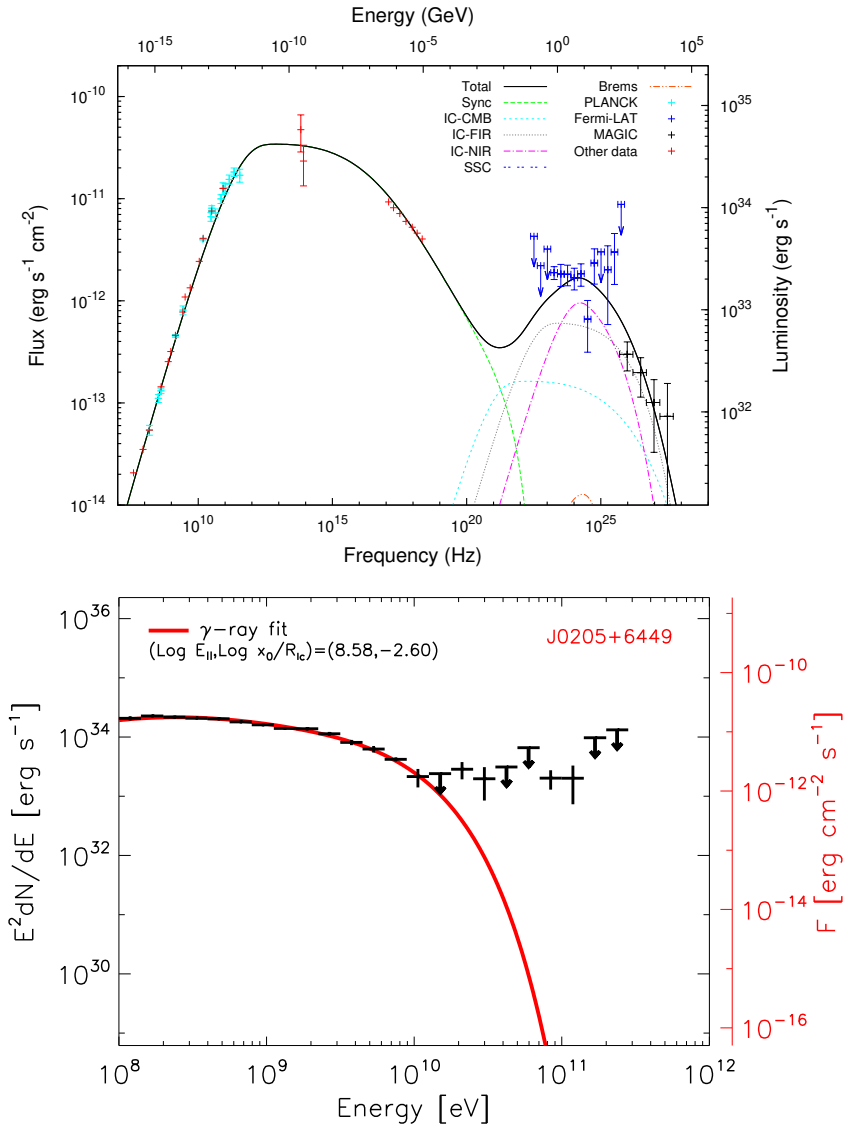

Figure 2.5: Top: Data for 3C 58 (including the MAGIC and derived off-peak data) compared with a time-dependent, energy-conserving PWN model prediction. The *Planck* data (cyan) are taken from Arnaud et al. (2016) while other data are taken from the compilation used by Torres et al. (2013). Bottom: phase-averaged SED compared with a synchro-curvature model. See text for details.

Chapter 3

Discovery and characterization of superefficiency in pulsar wind nebulae

Contents of this chapter

Here I numerically study the radiative properties of the reverberation phase of pulsar wind nebulae. Reverberation brings a significant evolution in a short period of time. We show that in some radiative models, even the Crab nebula, associated to the more energetic pulsar of the sample we consider, has a period in its future time evolution where the X-ray luminosity will exceed the spin-down power at the time. In fact, all nebulae in the sample herein studied are expected to have a period of radio, X-ray, and GeV superefficiency, and most will also have a period of TeV superefficiency. The first analysis and characterization of these superefficient phases is done here. This work was first published together with my supervisor, in The Astrophysical Journal Letters, Volume 864, Issue 1, article id. L2, 8 pp. (2018).

3.1 Introduction

Recently, [**?**] reported the discovery of a nebula surrounding the magnetar Swift J1834.9-0846. The fact that this system has the highest efficiency of all pulsar wind nebulae (PWNe) known was considered to be highly unusual: $\sim 10\%$ of the mild spin-down power of the pulsar, $L_{sd} \sim 10^{34}$ erg s^{-1}, is emitted just in soft X-rays. This promoted interpretations based on a transfer, via a yet unknown mechanism, of magnetic energy into particle acceleration (Granot et al. 2017). However, we demonstrated that the multifrequency data, as well as its size, could be encompassed by a normal, rotationally-powered PWN

under the condition that it is entering in reverberation (Torres 2017). The latter is a relatively short but important phase in the evolution of all PWNe, produced when the reverse shock created by the supernova explosion travels back toward the pulsar, compressing the wind bubble, see, e.g., Slane 2017, for a review. This compression heats the PWN, reducing its size, and increasing the magnetic field. Such evolution leads, as we see below, to an almost complete burn-off of the electron population. Despite the obvious importance of this phase, it is not yet usual that radiative models of PWNe consider it. In fact, the effect of reverberation upon the spectral results has been dealt with only in a few scattered occasions, and with different levels of detail, see, e.g., Gelfand et al. 2009, Vorster et al. 2013, Bandiera 2014, Bucciantini et al. 2011, Martin et al. 2016, Torres 2017 for different examples.

We aim at studying the radiative properties of the reverberation phase in detail. For this, we shall study the future reverberation period of well-characterized PWNe. We shall prove that the 10% efficiency found for Swift J1834.9-0846 is not a limit at any rate, not even for this very pulsar, finding that all PWNe can have periods of superefficiency from radio to gamma-rays.

3.2 PWN evolution

We use the code TIDE 2.3, which has been described in detail in Martin et al. 2016, Torres 2017. But here we add subroutines appropriate to compute efficiencies as a function of time, as described below. The main components and features of the model, apart that it takes into account the variation of the spin-down power, L_{sd}, according to a given value of braking index, n, are as follows:

- The injection function for pairs is assumed as a broken power law, powered by the pulsar. The model computes the time-evolution of the distribution subject to synchrotron, inverse Compton, and Bremsstrahlung interactions, adiabatic losses or heating, and accounting for escaping particles. Expressions for the radiative losses can be found in Martin et al. 2012.

- The magnetic field of the nebula is also powered by the rotational power (the instantaneous injection is the fraction of spin-down that goes to power the magnetic field, η). The field varies in time as a result of the balance between this power and the adiabatic losses or gains of the field due to the expansion or contraction of the PWN (Torres et al. 2013b).

- The size of the PWN is computed according to age, progenitor explosion energy, medium density, velocity, and pressure of the supernova ejecta at the position of the PWN shell. We take into account that the latter profiles change if the PWN

shell is surrounded by unshocked ejecta (thus the radius of the PWN is smaller than the radius of the reverse shock of the SNR, $R < R_{rs}$), or by shocked ejecta (where $R_{rs} < R < R_{snr}$, being R_{snr} the radius of the SNR). After reverberation, when the PWN pressure reaches that of the SNR, a Sedov expansion follows. Details are explicit in §3 of (Martin et al. 2016).

The theoretical approach described is able to cope well with multifrequency data of known nebulae. The red curves in the top panels of Fig. 3.1 shows the spectral energy distribution (SEDs) of the six PWNe (Crab, G09, G21, G54, Kes75, and J1834) that we take as examples in this work, at their corresponding age today as fixed or deduced from observations. The parameters for each model, together with the relevant pulsar's observational data are given in Table 1. Notation for all the parameters follows that usually found in the literature, and in any case, is consistent with that used by us before (Martin et al. 2016,Torres 2017). We divide parameters in Table 1 among measured or assumed, derived, and fitted values. Apart of these parameters we assume the following usual ones for all PWNe/SNR complexes: energy of the explosion $E_{SN} = 10^{51}$ erg, interstellar medium density $\rho_{ISM} = 0.5$ cm^{-3}, SNR density index = 9, PWN adiabatic index = 1.333, and SNR adiabatic index = 1.667. We also consider the cosmic microwave background with $T_{cmb} = 2.73$ K and $\omega_{cmb} = 0.25$ eV cm^{-3}). As expected, small variation in the fitted parameters are found when compared with similar models but that do not take into account reverberation (Torres et al. 2014).

Note that all PWNe studied are now relatively young, and considered to be free-expanding except for J1834. All other nebulae, such as Crab itself, will enter into reverberation sometime in their future. We choose these young nebulae (rather than other more mature) on purpose: as we shall see, reverberation is a very sensitive process, leading to a strong evolution where most of the electron population is wiped out. Since we are actually interested in the reverberation process itself, fixing the model parameters before this process happens makes more sense than doing it long after it ends.

Fig. 3.1 shows the time evolution of the model fitting the current data for each of the PWNe considered. The two sets of panels show the electron and spectral energy distributions along time. A strong time evolution is expected. The times shown are chosen within and around the corresponding reverberation period of each PWN, and correspond to the times of the maximum PWN radius, $t_1 = t(R_{max})$, the maximum of the X-ray efficiency, $t_2 = t(\mathrm{Eff}_X^{max})$, the minimum PWN radius, $t_3 = t(R_{min})$, and a later time already at the Sedov phase, $t_4 = t(@Sedov)$. Specific values for these times along the PWNe evolution of each nebula are also given in Table 1. The X-ray efficiency (and correspondingly, radio, GeV, and TeV efficiencies as well) are defined as the ratio of the luminosity emitted in a given frequency range at a given time with respect to the spin-down power at that same time, e.g., $\mathrm{Eff.}_X(t) = L_X(t)/L_{sd}(t)$. If at a time t we

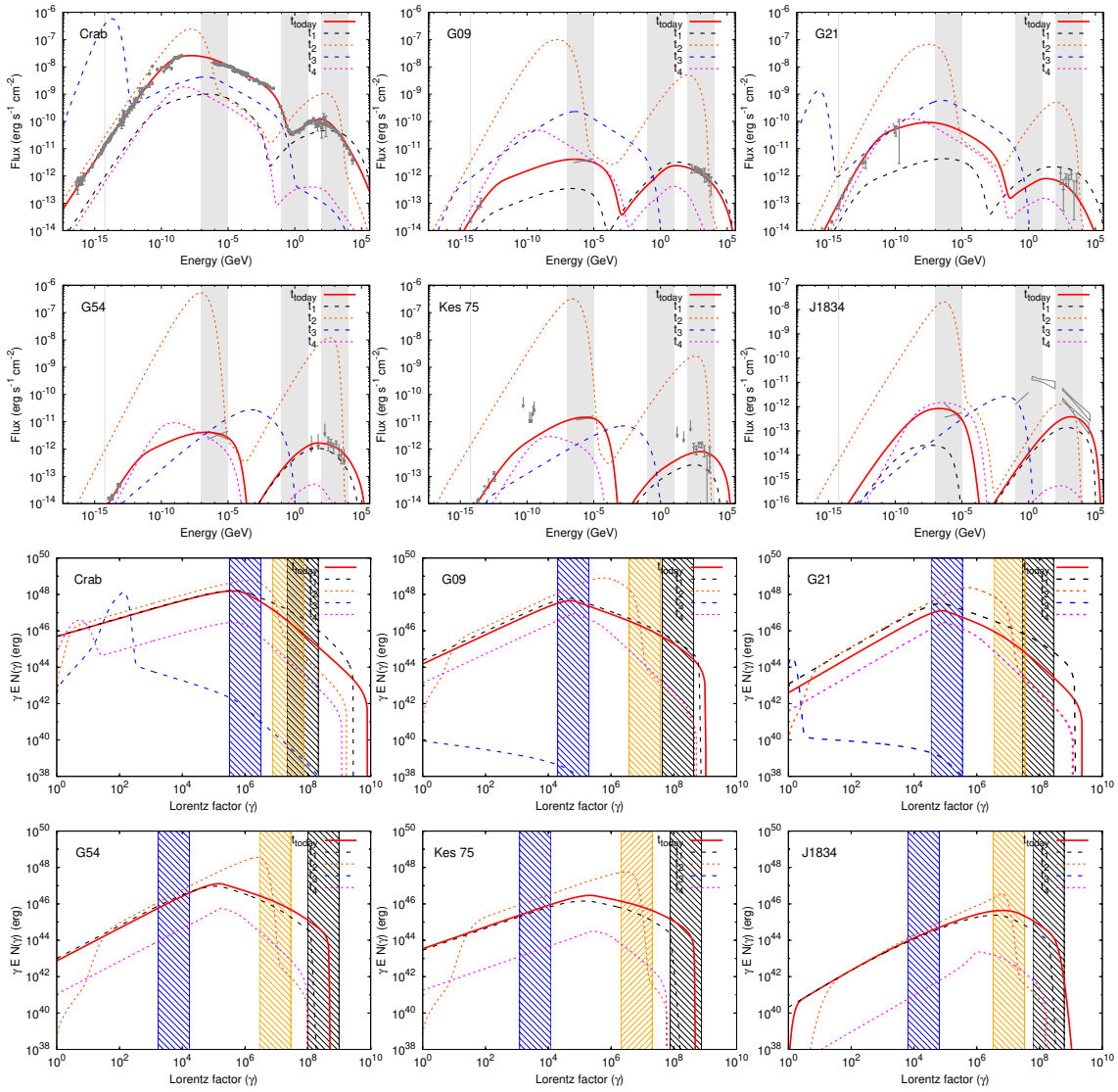

Figure 3.1: Spectral energy and electron distributions of the modelled PWNe along time. Each panel shows the evolution at different moments of interest for each nebula ($t_1 \ldots t_4$), which are introduced and discussed in the text, and includes also the results at the age today for comparison. The colored shadows in the electron panels note the Lorentz factor whose synchrotron-emitted characteristic energy is in the X-ray band (0.1–10 keV) for the nebular magnetic field value at t_1 (black), t_2 (orange) and t_3 (blue), respectively. The shadows in the SEDs note the radio (1.4 GHz), X-rays (0.1-10 keV), GeV (0.1-10 GeV), and TeV (1-10 TeV) bands used to compute the corresponding luminosities.

measure this ratio to be larger than 1, we shall say the PWN is superefficient.

3.3 Superefficiency

Fig. 3.2 shows the time evolution of the calculated efficiencies in radio (1.4 GHz), X-rays (0.1-10 keV), GeV (0.1-10 GeV), and TeV (1-10 TeV), together with the PWN radii. Table 1 shows the timescale for the duration of reverberation ($t(R_{min}) - t(R_{max})$), the minimum radius, and the maximum magnetic field attained, as well as the properties of any superefficiency period in radio, X-rays, GeV, or TeV energies (maximum efficiency, Eff.^{max}; duration, Dos; and the time at which the maximum efficiencies happen, t(Eff.^{max})). We also show the time t_4 in the Sedov expansion used in the figures as an example of the spectra in this regime, and values of the magnetic field at different times of interest. Reverberation brings a significant evolution in a short period of time. Plotting efficiencies rather than distributions makes this evolution more clear.

The X-ray efficiency has several stages of increase and decrease, which can be used to define different phenomenological phases. We call them phases a to c, for reference. We distinguish these phases via the following subsequent events: Phase a has the PWN in free expansion, and lasts from the pulsar birth to the maximum of the nebula radius (at t_1). Phase b finishes at the maximum of the X-ray efficiency (at t_2). Phase c finishes at the minimum of the radius (at t_3). Phase d is the Sedov expansion, assumed to continue after t_3. We use different background colours in Fig. 3.2 to distinguish these phases. Their spectral and electron properties at these times were shown in Fig. 3.1. Note that in some cases, phase c is too short to be visible without a zoom in the reverberation period, as shown in the second and fourth rows of Fig. 3.2.

Fig. 3.2 shows that even the Crab nebula, associated to the more energetic pulsar of the sample we study, has a period in its future time evolution where, e.g., the X-ray luminosity will exceed the spin-down power at the time. In fact, all PWNe in our sample are expected to have a period of radio, X-ray, and GeV superefficiency, and all but Crab and J1834, will also have a period of TeV superefficiency. The finding of superefficiency at all frequencies dramatically shows how dangerous it is to rule out a pulsar of a given spin-down power as a possible origin of nebula whose radio, X-ray, GeV, or even TeV luminosity exceeds it.

The zoomed panels in Fig. 3.2 show that the moments at which the maximum efficiencies are attained are close but not exactly the same at different frequencies. This is a natural result of having electrons of different energies contributing to the photon spectrum at different frequencies. The number of electrons at a given energy is in turn a result of a balance between gains (via adiabatic heating) and losses (via radiation and escape) and the peak number is attained at different times for different energies. We also

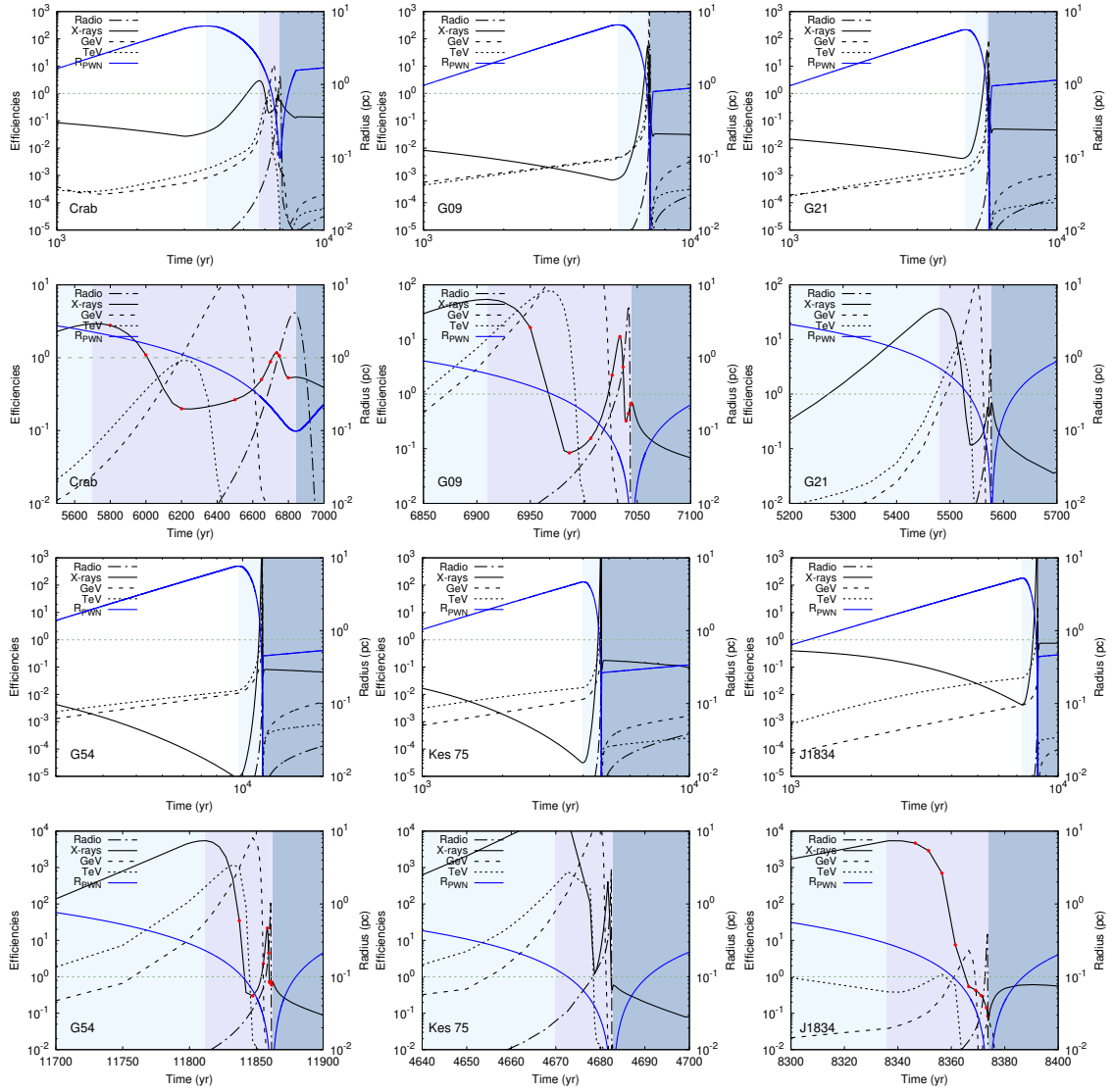

Figure 3.2: Evolution of the PWNe efficiencies in X-rays (0.1-10 keV), GeV (0.1-10 GeV), and TeV (1-10 TeV) and PWN radii along time. The second and fourth rows zooms around the reverberation period, as shown in the corresponding global evolution panels.

note that there is a variety of possibilities regarding which of the maximum efficiencies is the largest. Sometimes, like the case of J1834 and Kes 75, the largest maximum efficiency occurs for the X-rays. In others, for more energetic pulsars like Crab, G09, or G21, it occurs at the GeV band. The evolution of the radio efficiency is quite similar for all PWNe. It shows a sharp peak happening close to the time of maximum of the compression. In this small time scale around t_3, all the PWNe studied become superefficient in radio. However, the maximum efficiency attained in the radio band is typically smaller than that reached at higher frequencies, see Table 1.

The zoomed panels of Fig. 3.2 can actually be considered as a proxy for the evolution of the luminosities themselves, in arbitrary units. In such a short period of time, the change of the spin-down power is small. In these zoomed panels, we note the appearance of a second peak in the X-ray efficiency for most of the cases studied (of which those appearing in Crab and G09 are examples). When such second peak happens, it is closer to the time of the minimal radius. Whereas this second peak is however only a local maximum, with the absolute largest X-ray efficiency happening at earlier times, it may also provide a second –and shorter– superefficiency period in some cases.

In the zoomed panels of Fig. 3.2, we marked on some exemplary cases (Crab, G09, G54, and J1834) several times of interest between the times of the maximum of the X-ray efficiency and its second local maximum. At these times, we plotted the electron distribution, the synchrotron and self-synchrotron Compton contribution to the photon spectrum in Fig. 3.3. This figure shows how the synchrotron-related processes dominate the shape of the spectrum at both low and high energies (compare Fig. 3.3 with the corresponding total SED shown in Fig. 3.1). This is particularly obvious when the two peaks in the SED appear clearly distinguished in energy, at the time of maximum efficiency t_2.

We note that the maximum of the X-ray efficiency does not occur at the minimum of the radius, but at a time in between the start of reverberation and the latter. This is in remarkable agreement with a result from analytical considerations earlier done by Bandiera (2014). This happens in all cases studied, and is a result of the energetic balance: a competence between electron heating by the nebular compression and how fast electrons escape or are cooled down via the emission of synchrotron radiation. The more compressed is the nebula, electrons are cooled down faster (via synchrotron radiation in a larger magnetic field), and a smaller number of electrons are actually available to emit in X-rays. The competition between gains by adiabatic heating and losses by synchrotron along the critical time period is shown in Fig. 3.4. They depict the timescales for energy gains and losses at the same times in which the corresponding SEDs and electron distributions were shown earlier. It can be seen that during most of the compression, synchrotron radiation has a shorter timescale than heating for the Lorentz factors of interest, and

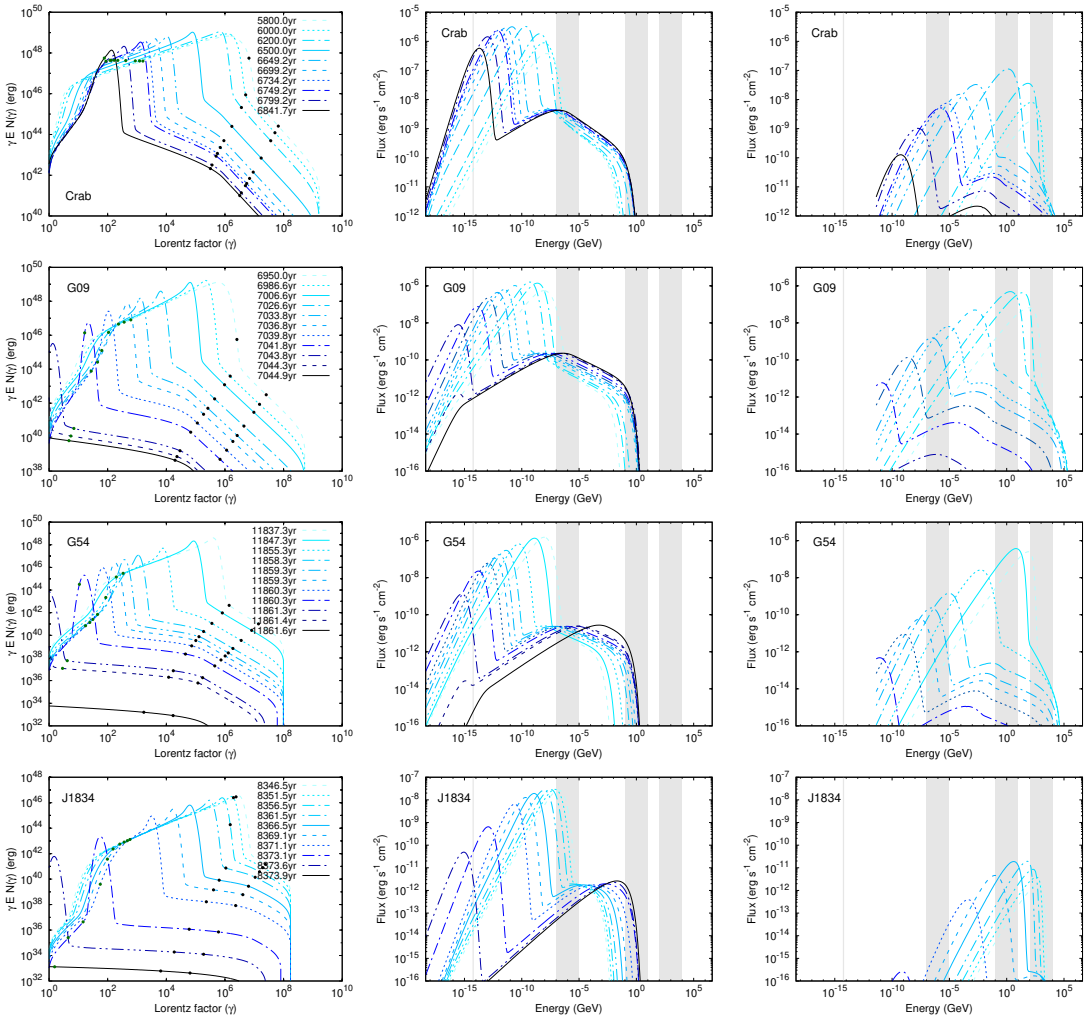

Figure 3.3: Details of the time evolution of the electron distribution and the synchrotron and self-synchrotron Compton contribution to the photon spectrum around the time of minimum radii and maximum efficiency, between t_2 and t_3 in the corresponding panels of Figure 3.1. Times are color-coded as described in the left panels.

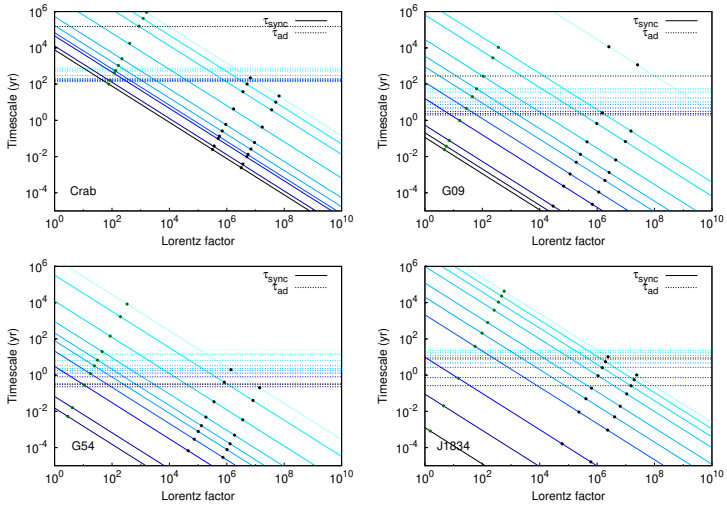

Figure 3.4: Timescales for the adiabatic heating and the energy losses via synchrotron radiation. The black dots mark the interval of Lorentz factors emitting synchrotron photons with characteristic energies in the X-ray band. The green dot marks the same for radio (synchrotron photons with characteristic energies at 1.4 GHz). The curves are color-coded as in Fig. 3.3.

quickly burns off the electron population in all PWNe. This is consistent with the SEDs being dominated by synchrotron and self-synchrotron emission, and with the appearance of a second peak in the X-ray efficiency, as further discussed below.

Fig. 3.3 and 3.4 also show the interval of Lorentz factors emitting synchrotron photons with characteristic energies ($\nu_c = (3/4\pi)\gamma^2(eB/mc)$) between 0.1 and 10 keV (noted with black dots), and radio (1.4 GHz, noted with green dots). The Lorentz factors of interest for the emission of photons at these bands change significantly along the time evolution, even in this limited time extent, due to the strong variation in the magnetic field. This was also summarily shown in Fig. 3.1, where we showed these intervals at $t_2 = t(\mathrm{Eff}_X^{max})$ and $t_3 = t(R_{min})$. For these Lorentz factors of interest, and along the period shown, the number of electrons uniformly decreases, due to the cooling domination.

At the beginning of phase c the peak of the synchrotron contribution to the SED, shown in the middle panel of Fig. 3.3, is close to the X-ray band of interest, affecting the value of efficiency just as a consequence of the band selection. If, instead, we would be interested in the hard X-ray luminosity above 100 keV, the X-ray synchrotron flux would uniformly increase with time.

In addition of the X-ray luminosity variation via synchrotron, the X-ray flux is also affected by self-synchrotron emission, see the second and third panels of Fig. 3.3. The

latter radiation process dominates the production of the second peak. It happens at times when the comptonized synchrotron spectrum actually peaks in X-rays instead than in gamma-rays. When it does, the flux in X-rays produced by self synchrotron Compton emission may be one order of magnitude larger than that produced by synchrotron emission directly. This emphasizes how important it is to consider the self-synchrotron Compton process along the evolution of all nebulae, even when at later times it may be, usually, completely irrelevant.

Note that when they happen, these second peaks occur closer to (but still before) the minimum of the radius. Note too that the GeV (and TeV) maximum efficiency happens always after the X-ray one. The reason for all this is the same, and is related to the fact that the self-synchrotron emission, which we compute following with the formulae given in the Appendix of Martin et al. (2012), is quadratic in the number of electrons, inversely quadratic in the size of the nebula, and linear in the field. The electrons influence is thus larger for self-synchrotron emission, given that they are also accounted in the photon target distribution. However, the maximum efficiency moves towards later times when compared to the X-ray one since for a longer time the reduction of particles is compensated by the increase in the field and the decrease in the radius. With reverberation wiping electrons off quickly, once the maximum of the GeV luminosity is attained and starts to decrease, there is no possible compensation to the loss of electrons. There is no second peak in GeV or TeV energy bands because at these energy bands there is only one dominant process generating the SED, and the recovery can only happen when a sufficient number of high energy electrons are rebuilt by the pulsar.

3.4 Concluding remarks

Here, we have shown that supereffiency periods in which the luminosity at a given band from radio to TeV exceeds the pulsar spin-down power, are common. They are unavoidably associated with the reverberation process. Supereffiency happens because when the PWNe are reverberating, the spin-down power is no longer the energy reservoir. In these cases, the nebulae are receiving energy from the environment, and the spin-down power is, a priori, not determinant to judge detectability at any band.

Observing one such superefficient system would be amazing: a bright, small or point-like nebula, with a spatially coincident pulsar many times less energetic. The difficulty for observing them is that such systems can be maintained only for a few hundred years. For the estimate that follows, let us assume that the superefficiency period roughly lasts about 300 years in the evolution of young nebulae, of typically < 10000 years of age (although note that as the G54 case tells, supernova with large ejected masses or low density environments can produce reverberation beyond this age). Assuming a pulsar

birthrate of 3 century^{-1} (Faucher et al. 2006), 300 PWNe were born within the last 10000 years, and from these, we are interested in a period equivalent to –at most– 3% of their evolution. Taking into account the correspondingly shorter percentages for pulsars born at different centuries, we have a probability of $\sim 1\%$ of finding one these pulsars in the right period of their evolution. Thus we expect at most 3 PWNe in a superefficient stage in the Galaxy today. This should be taken rather as an upper limit, because it assumes it is equally probable to have reverberation at any time within the first 10000 years of a pulsar (thus neglecting that there is no reverberation in their free-expansion phases).

Note that our model assumes no morphological shape for the PWN; they are described with a time-varying radius. If the compression is asymmetric or turbulence develops, superefficiency could be less effective, detaining the reduction in the PWN size and the increment in the field perhaps before our results indicate. This might affect less energetic nebulae in particular, such as Kes 75 or J1834, being likely unimportant for others such as G09, G21 or Crab. Magneto-hydrodynamical simulations will verify on this issue. In any case, R_{min} is many orders of magnitude larger than the pulsar's radius, or even the pulsar's magnetosphere (typically at least 6 orders of magnitude larger than the size of a young pulsar's light cylinder), and thus the inner workings of the pulsed emission via synchro-curvature radiation (as the one used in the previous chapter), is not expected to be significantly affected even in the most severe of the compressions.

Table 3.1: Physical parameters used by, and resulting from the fits.

PWN		Crab Nebula	G0.9+0.1	G21.5-0.9	G54.1+0.3	G29.3-0.3	J1834.9-0846
referred to as		Crab	G09	G21	G54	Kes 75	J1834
Measured							
t_{age}	[years]	960	2000	870	1700	700	7970
$P(t_{age})$	[ms]	33.40	52.2	61.86	136	324	2480
$\dot{P}(t_{age})$	[s s^{-1}]	4.2×10^{-13}	1.5×10^{-13}	2.0×10^{-13}	7.5×10^{-13}	7.1×10^{-12}	7.96×10^{-12}
n	...	2.509	3	3	3	2.16	2.2
D	[kpc]	2.0	8.5	4.7	6	6	4
Derived							
τ_0	[years]	758	3305	3985	1171	547	280
B_s	[G]	4.68×10^{12}	2.91×10^{12}	3.58×10^{12}	1.01×10^{13}	8.19×10^{13}	1.43×10^{14}
$L_{sd}(t_{age})$	[erg s^{-1}]	4.5×10^{38}	4.3×10^{37}	3.4×10^{37}	1.2×10^{37}	8.2×10^{36}	2.1×10^{34}
L_0	[erg s^{-1}]	3.0×10^{39}	1.1×10^{38}	5.0×10^{37}	7.2×10^{37}	7.7×10^{37}	1.74×10^{38}
Fitted							
M_{ej}	[$M_\odot$]	9.0	11	8	20	6	11.3
T_{fir}	[K]	70	30	35	20	25	25
ω_{fir}	[eV cm^{-3}]	0.1	2.5	1.4	2.0	2.5	0.5
T_{nir}	[K]	5000	3000	3500	3000	5000	3000
ω_{nir}	[eV cm^{-3}]	0.3	25	5.0	1.1	1.4	1.0
γ_b	...	9×10^5	1.0×10^5	1.0×10^5	5.0×10^5	2.0×10^5	1.0×10^7
α_l	...	1.5	1.4	1.0	1.2	1.4	1.0
α_h	...	2.54	2.7	2.5	2.8	2.3	2.1
ϵ	...	0.27	0.2	0.2	0.3	0.2	0.6
η	...	0.02	0.01	0.04	0.005	0.008	0.045
Outcomes							
Rev. Timescale	[years]	3201.7	1703.9	1028.86	2242.61	674.679	1037.906
$t_1 = t(R_{max})$	[years]	3640	5341	4549	9619	4007	7336
r_{min}	[pc]	9.8×10^{-2}	3.2×10^{-3}	7.3×10^{-3}	1.3×10^{-4}	7.5×10^{-5}	5.5×10^{-4}
$B_{max} = B_{t_3}$	[G]	5.6×10^{-2}	14.7	4.7	2.0×10^3	3.9×10^3	1.4×10^2
$\text{Eff.}_{\text{r}}^{max}$	...	4.1	41.9	7.2	106.9	905.5	14.9
Dos_{r}	[years]	150	12.2	4.0	4.0	3.9	1.0
$t(\text{Eff.}_{\text{r}}^{max})$	[years]	6834.2	7041.8	5575.8	11860.8	4682.5	8373.5
Eff._X^{max}	...	2.9	54.2	36.8	5464	23523	5444
Dos_X	[years]	800	327	237	342	129	316
$t_2 = t(\text{Eff}_X^{max})$	[years]	5700	6900	5450	11807	4668	8337
$\text{Eff.}_{\text{GeV}}^{max}$	...	11.7	1180	100.8	6541	22681	5.5
Dos_{GeV}	[years]	439	127	67	58	24	8
$t(\text{Eff}_{\text{GeV}}^{max})$	[years]	6500	7007	5547	11847	4680	8366
$\text{Eff.}_{\text{TeV}}^{max}$	...	0.9	72.4	6.6	1193	0.01	1.00
Dos_{TeV}	[years]	...	92	37	147	29	5
$t(\text{Eff.}_{\text{TeV}}^{max})$	[years]	6250	6960	5510	11832	4680	8356
$t_3 = t(R_{min})$	[years]	6841.7	7044.9	5577.9	11861.6	4682.7	8373.9
$t_4 = t(@Sedov)$	[years]	8011.4	8002.9	5993.1	13025.7	5007.6	8988.8
B_{t_4}	[G]	2.2×10^{-4}	2.2×10^{-4}	2.7×10^{-4}	1.7×10^{-4}	3.0×10^{-4}	2.1×10^{-4}
B_{today}	[G]	1.1×10^{-4}	1.4×10^{-5}	8.5×10^{-5}	1.2×10^{-5}	2.5×10^{-5}	4.9×10^{-6}

Chapter 4

Towards observing reverberating and superefficient pulsar wind nebulae

Contents of this chapter

In the last chapter we numerically study the radiative properties of the reverberation phase of PWNe, i.e., when the reverse shock created by the supernova explosion travels back towards the pulsar, compressing the wind bubble. We focused on several well-characterized PWNe and used them as examples for introducing the concept of superefficiency. The latter is a period of the PWN evolution, happening within reverberation, where the luminosity in a given band exceeds the spin-down power at the time. Here, we explore a broad range of PWN models to study their reverberation and superefficiency phases in a systematic way. Armed with these models we consider two aspects: On the one hand, we analyze via Monte Carlo simulations how many Galactic PWNe are expected to be reverberating or in a superefficiency stage at any given time, providing the first such estimations. On the other hand, we focus on searching for observational signatures of such periods. We analyze archival observations and check for the existence of possible candidates for superefficient PWNe. We also provide predictions for the future evolution of the magnetar nebula J1834.9-0846 (which we consider to be starting its reverberation period) along the next 50 years. Using our simulations as input we study how sensitive current and future X-ray satellites (like *eXTP* or *Athena*) will be to observe such evolution, concluding that they will be able to track it in detail. This work has been published originally with my collaborators in the group in Monthly Notices of the Royal Astronomical Society, Volume 486, Issue 1, p.1019-1033 (2019).

4.1 Introduction

As we studied earlier, everberation is a short but important phase in the evolution of all pulsar wind nebulae (PWNe), produced when the reverse shock created by the supernova explosion travels back towards the pulsar, compressing the wind bubble. Its impact on the PWN evolution has been studied - by Gelfand et al. 2009, Vorster et al. 2013, Bandiera 2014, Bucciantini et al. 2011, Martin et al. 2016, Torres 2017, and this thesis, although it is not usual that radiative models used to interpret observations take it into account yet (see Gelfand 2017 for a review). When reverberation happens, the PWN size decreases, the magnetic field increases, and the medium transfers energy to the PWN rather than the other way around. Neither the instantaneous spin-down power of the pulsar nor the integrated rotational power up to this point in the nebula evolution is the energy reservoir in this period. The transfer of energy occurs via adiabatic heating of the particles in the nebula. Upgraded in energy, particles emit at higher frequencies. Because of the size reduction and magnetic field increase, the suddenly heated particles encounter appropriate conditions for radiative cooling via synchrotron and self-synchrotron emission. This leads to a quick burn out of the particle population together with a concurrent increase of luminosity.

Before we showed that even the Crab nebula, associated to the more energetic pulsar of the sample then considered, will have its X-ray luminosity exceeding the spin-down power at a certain time of its future evolution. We dubbed this period in the life of nebulae as the superefficient stage and characterized its main properties. However, a systematic exploration of the superefficiency and reverberation periods was still lacking. Also lacking was an estimation of the number of systems that could be in such superefficient, or in general, in a reverberation period, at any given time in our Galaxy. These two tasks are undertaken in this work. In order to achieve these results, we produce a set of systematic, and equally detailed PWNe simulations, and compare their reverberation periods as a function of the pulsar energetics and their different environmental properties. Using these PWN evolutionary tracks, as well as current knowledge of the pulsar population and their birth rate, we compute the number of reverberating and superefficient PWNe via Monte Carlo simulations. The final part of this work deals with the observational signatures of such periods. We analyze archival observations to see whether possible candidates of superefficient PWNe could have been already observed. We also provide predictions for the future evolution of the nebula around the magnetar J1834.9-0846, which is considered to be starting its reverberation period (see Torres 2017), along the next 50 years. Using our simulations as input we finally study how well future X-ray satellites (like *eXTP* or *Athena*) will be able to observe such evolution.

4.2 Systematic exploration of superefficiency and reverberation

When compared to one another, real PWNe are subject to different environmental properties. In order to compare generic reverberation and superefficiency properties for different pulsars in a more sensitive way, here we shall simulate putative PWNe generated by pulsars that differ from one another only in their energetics. Particularly, we shall assume that the values of the initial spin-down power, L_0, of these putative pulsars are a multiple of that shown by a specific *real* pulsar anchor (e.g., the Crab pulsar), but that they have the same braking index, n, initial spin-down age, τ_0, and environmental variables of the latter. (see the previous chapter for the fitted values of the mass of the ejecta, the photon energy densities, and other parameters for a few examples of known and well-characterized PWNe). Then, we shall obtain the spin-down power, $L_{sd}(t)$, and relate the initial spin-down age with the characteristic age, $\tau_c(t)$, as a function of time, as follows

$$L_{sd}(t) = L_0 \left(1 + \frac{t}{\tau_0}\right)^{-\frac{n+1}{n-1}}, \tag{4.1}$$

$$\tau_0 = \frac{2\tau_c(t)}{n-1} - t \tag{4.2}$$

Additionally using the equations defining the characteristic age and spin-down (Pacini et al. 1973, Gaensler & Slane 2006),

$$\tau_c(t) = \frac{P(t)}{2\dot{P}(t)}, \tag{4.3}$$

$$L_{sd}(t) = \frac{4\pi^2 I \dot{P}(t)}{P(t)^3}, \tag{4.4}$$

we can derive the time evolution of P and $\dot{P}$:

$$P(t) = \sqrt{2\pi^2 \frac{I}{\tau_c(t) L_{sd}(t)}}, \tag{4.5}$$

$$\dot{P}(t) = \frac{1}{2}\frac{1}{\tau_c(t)}\sqrt{\frac{2\pi^2 I}{\tau_c(t) L_{sd}(t)}}. \tag{4.6}$$

These equations will track the evolution of the pulsars in the $P\dot{P}$-diagram (see Fig. 4.1 and Table 1). PWNe simulations are done using the code Tide 2.3, presented in Martin et al. (2016). Their radiative content can be found in Martin et al. 2012, details on the treatment of the nebula magnetic field in Torres et al. 2013, and of the initial free expansion phase as well as its systematic application to young PWNe in Torres et al. 2014. In particular, we are using a broken power law to describe the injected particles and consider that the variation of the magnetic energy in the PWN is balanced by the fraction of the rotational energy that powers the magnetic field (instantaneous power into the field is given by $\eta L(t)$, where η is the magnetization) and the adiabatic losses due to the expansion of the PWN. See equations 4 and 11 of Martin et al. 2016.

4.2.1 Details on the simplified dynamical evolution

Given the importance of the assumptions related to how the radius is computed along the dynamical evolution, we shall briefly summarize again here the prescription included in our PWN model.

Assuming that v, R, M and P are the velocity, radius, mass and pressure in the PWN bubble; and that v_{ej}, ρ_{ej} and P_{ej} correspond to the values of the velocity, density, and pressure of the SNR ejecta at the position of the PWN shell, we compute the radius of the PWN during the free expansion phase and compression by solving the equations given by Chevalier (2005), using a similar prescription as in Gelfand et al. (2009):

$$\frac{dR(t)}{dt} = v(t), \tag{4.7}$$

$$M(t)\frac{dv(t)}{dt} = 4\pi R^2(t)\left[P(t) - P_{ej}(R,t)\right], \tag{4.8}$$

$$\frac{dM(t)}{dt} = 4\pi R^2(t)\rho_{ej}(R,t)(v(t) - v_{ej}(R,t)); \tag{4.9}$$

$$\text{for } v_{ej}(R,t) < v(t), \tag{4.10}$$

$$\frac{dM(t)}{dt} = 0;\ \text{for } v_{ej}(R,t) \geq v(t) \tag{4.11}$$

To account for the radiative (as well as other) losses by the particles inside the PWN in the computation of the PWN pressure $P(t)$, we solve the diffusion-loss equation

$$\frac{\partial N(\gamma,t)}{\partial t} = Q(\gamma,t) - \frac{\partial}{\partial\gamma}\left[\dot{\gamma}(\gamma,t)N(\gamma,t)\right] - \frac{N(\gamma,t)}{\tau(\gamma,t)}, \tag{4.12}$$

The terms on the right hand side take into account the radiative energy losses, the losses or energy gains by compression or expansion of the PWN, and the escape of particles (we assume Bohm diffusion), for which $\tau(\gamma,t)$ is here the timescale. We solve Eq. 4.12 in each time-step and compute the total energy contained in pairs, E_p, by doing the integral,

$$E_p(t) = \int_{\gamma_{min}}^{\gamma_{max}} \gamma m_e c^2 N(\gamma,t)\mathrm{d}\gamma. \tag{4.13}$$

The pressure contributed by particles is

$$P_p(t) = \frac{3(\gamma_{pwn}-1)E_p(t)}{4\pi R(t)^3}. \tag{4.14}$$

γ_{pwn} is the adiabatic coefficient of the PWN relativistic gas, which is fixed as 4/3. The magnetic pressure is

$$P_B(t) = \frac{B^2(t)}{8\pi}. \tag{4.15}$$

And finally, the total pressure is

$$P(t) = P_p(t) + P_B(t). \tag{4.16}$$

In this prescription, the v_{ej}, ρ_{ej} and P_{ej} change if the PWN shell is surrounded by unshocked ejecta ($R < R_{rs}$), or by shocked ejecta ($R_{rs} < R < R_{snr}$, being R_{snr} the radius of the SNR). The initial profiles for the unshocked medium are assumed, following Truelove et al. (1999), Blondin 2001, as

$$v_{ej}(r,t) = \begin{cases} r/t & \text{for} \quad r < R_{snr}, \\ 0 & \text{for} \quad r > R_{snr}, \end{cases} \tag{4.17}$$

$$\rho_{ej}(r,t) = \begin{cases} A/t^3 & \text{for} \quad r < v_t t, \\ A(v_t/r)^{\omega} t^{\omega-3} & \text{for} \quad v_t t < r < R_{snr}, \\ \rho_{ism} & \text{for} \quad r > R_{snr}, \end{cases} \tag{4.18}$$

$$P_{ej}(r,t) = 0, \tag{4.19}$$

where

$$A = \frac{(5\omega - 25)E_{sn}}{2\pi\omega v_t^5}, \tag{4.20}$$

$$v_t = \sqrt{\frac{10(\omega-5)E_{sn}}{3(\omega-3)M_{ej}}}. \tag{4.21}$$

The parameters E_{sn} and M_{ej} are the energy of the SN and the total ejected mass during the explosion, respectively. In our model, for simplicity, we assume $\omega = 9$ as in Chevalier 1992, Blondin 2001, Gelfand et al. 2009 for a type II SN. We have however tested that changing this steep decline of the density by using another power law index, e.g., $\omega = 6$ the start of the reverberation is slightly affected, but the extent of the compression is maintained.

When the PWN shell is surrounded by the shocked medium, then we use the appendix of Bandiera (1984) to obtain the v_{ej}, ρ_{ej} and P_{ej} profiles.

For the shock trajectories, we use the semianalytic model by Truelove and McKeee (1999) for a non-radiative SNR.

The rebounce after the compression is treated with an ad hoc pasting into a Sedov expansion, i.e., we consider that the PWN bounces and starts the Sedov phase when its pressure reaches the pressure of the SNR's Sedov solution and that at this time, the evolution of the radius of the PWN follows the relation given in Bucciantini et al. (2011)

$$R^4(t_{Sedov})P(t_{Sedov}) = R^4(t)P(t), \tag{4.22}$$

where $P(t) = \rho_{ism} v_{fs}^2/(\gamma_{snr}+1)$ is the pressure in the SNR forward shock. The term v_{fs}^2 is the velocity of the forward shock given by the Truelove & McKee equations.

4.2.2 Sample

We shall consider here four different specific cases of pulsar anchors for generating the models: the magnetar J1834.9-0846 (referred to as J1834), Crab, G0.9+0.1 (G09), and

G54.1+0.3 (G54). We shall especially consider initial spin-down powers ranging from $L_0 \sim 10^{35}$ to 10^{40} erg s^{-1} (see below for further discussion on this point). Our earlier chapter gives the parameters for the anchor pulsar and PWN properties, e.g., their braking index and the observational values for the current P and $\dot{P}$, as well as resulting features of their evolution (e.g., the duration of reverberation and of any superefficiency found in the energy ranges explored). Table 1 here gives the L_0 values considered for each of the simulated models based on these real PWNe, whereas all other parameters of the simulated PWNe are assumed as the corresponding original ones quoted in the previous chatper. The latter also applies to fitted parameters of the real PWNe, like the magnetization or the break energy.

We analyze 10 models for each of the anchor nebulae considered, and evolve each of them up to more than 20000 years of age in order to see how the whole reverberation process comes to an end and the continuing evolution thereafter. Thus, each observed PWNe is assumed to generate a family of models obtained by changing their initial spin-down power. These families are explicitly shown in Fig. 4.1. The gridding used for the family conformation is admittedly coarse, but as can be seen in the figure (see the separation of the red dots and the corresponding evolutionary tracks) it already covers quite well the space of interest.

Table 1 also gives the maximal X-ray efficiency achieved, the PWN age at which the X-ray maximal efficiency happens, the duration of the corresponding superefficient X-ray period as well as the starting and end of this period, (Dos$_{\rm X}$, $t_{\rm start-X}$, $t_{\rm end-X}$), and the same for the whole reverberation process (Dor, $t_{\rm start-R}$, $t_{\rm end-R}$). Models noted in red in Table 1 represent the values of the real, and corresponding anchor PWNe. Given that we are not interested in fitting any particular observational data, we shall not present here the evolving SEDs or the electron spectrum for the simulated PWNe, but report on the properties of the reverberation period only. Fig. 4.2 gives the evolution of the X-ray efficiency (in the 0.1–10 keV band) as a function of time for the models considered. We use these evolutionary plots next to determine the reverberation and superefficiency properties of these PWNe.

4.2.3 Results

The results for the superefficiency interval are summarized in Fig. 4.3 and Table 1.

The PWNe depicted in Fig. 4.3 are similar in all respects (in particular, evolving in the same environment) to each of the corresponding anchor-PWN quoted in the labels of the panels, but have varying initial spin-down power, see Table 1. There, the crosses along the curves of each panel show the properties of the superefficiency period of the real PWN, as modelled before. The dots along the curves represent the different models studied here, and are color-coded as in Fig. 1, with the lightest color assigned to the smallest initial

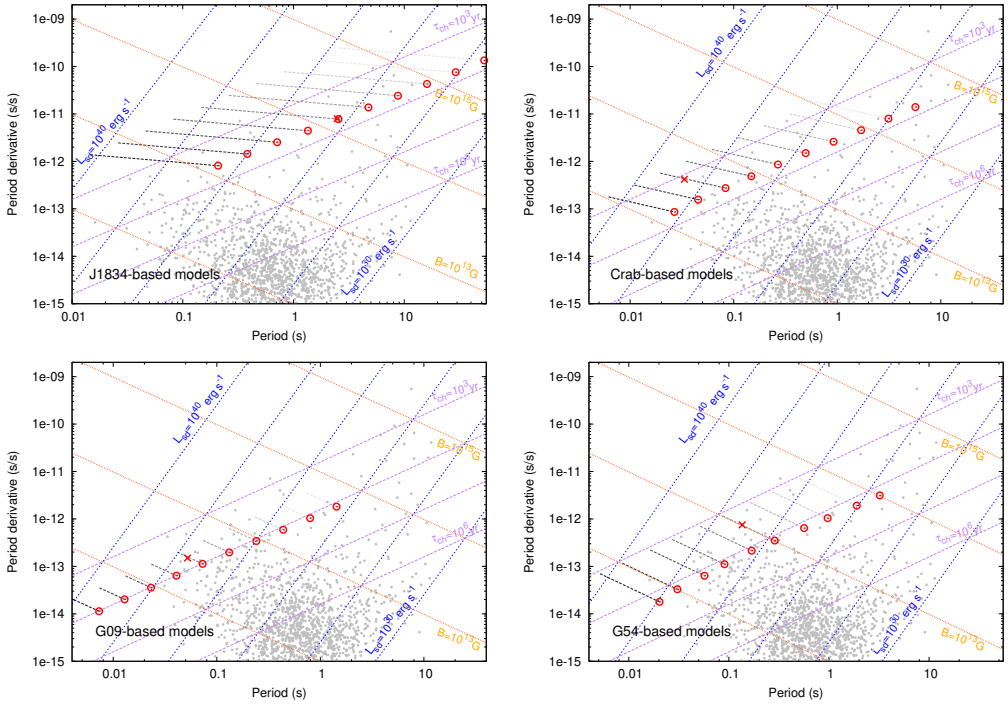

Figure 4.1: $P\dot{P}$-diagram for pulsars models using different anchor PWNe, as noted. The blue dashed lines represent an equal value of spin-down power, shown in increasing factors of 10^2. The orange and purple lines represent equal values of magnetic field and characteristic age, respectively, both are shown in increasing factors of 10. The grey points are known radio pulsars, obtained from the ATNF Catalog (Manchester et al. 2005). The red crosses represent the current values of the corresponding anchor nebulae, whereas the hollow circles represent the values of P and $\dot{P}$ at the moment of maximum X-ray efficiency for each of the models. The gray lines joining the red circles are the traces along their evolution. They are color-coded such that the darkest one represent pulsars with the highest initial spin-down power. See text for further discussion.

Table 4.1: Models of PWNe. See text for a discussion.

anchor PWN:			J1834.9-0846	Crab	G0.9+0.1	G54.1+0.3
model 1	L_0	[erg s^{-1}]	1.7×10^{40}	3.0×10^{40}	1.1×10^{40}	2.0×10^{40}
	Max. Eff.$_X$	...	7.9	0.4	0.02	0.07
	t(max.eff)$_X$	[years]	6550.0	5850.0	6900.0	16800.0
	Dos$_X$	[years]	1909.0	0	0	0
	$t_{\rm start-X}$	[years]	5141.0	0	0	0
	$t_{\rm end-X}$	[years]	7050.0	0	0	0
	Dor	[years]	3282.3	5879.0	0	11180.0
	$t_{\rm start-R}$	[years]	4370.0	3788.0	0	9991.0
	$t_{\rm end-R}$	[years]	7652.3	9667.0	0	21171.0
model 2	L_0	[erg s^{-1}]	5.5×10^{39}	9.5×10^{39}	3.5×10^{39}	7.2×10^{39}
	Max. Eff.$_X$	...	85.8	0.3	0.05	0.3
	t(max.eff)$_X$	[years]	6750.0	5400.0	6800.0	13550.0
	Dos$_X$	[years]	1146.0	0	0	0
	$t_{\rm start-X}$	[years]	5804.0	0	0	0
	$t_{\rm end-X}$	[years]	6950.0	0	0	0
	Dor	[years]	1963.3	5303.0	4619.0	10243.0
	$t_{\rm start-R}$	[years]	5092.0	3423.0	4293.0	6878.0
	$t_{\rm end-R}$	[years]	7055.3	8726.0	8912.0	17121.0
model 3	L_0	[erg s^{-1}]	1.7×10^{39}	3.0×10^{39}	1.1×10^{39}	2.0×10^{39}
	Max. Eff.$_X$	...	507.7	2.9	0.2	2.6
	t(max.eff)$_X$	[years]	7150.0	5700.0	7000.0	13100.0
	Dos$_X$	[years]	674.3	907.6	0	2103.0
	$t_{\rm start-X}$	[years]	6566.3	5142.4	0	11797.0
	$t_{\rm end-X}$	[years]	7240.6	6050.0	0	13900.0
	Dor	[years]	1400.4	3200.7	4208.0	8386.0
	$t_{\rm start-R}$	[years]	5880.0	3641.0	4236.0	6680.0
	$t_{\rm end-R}$	[years]	7280.4	6841.7	8444.0	15066.0
model 4	L_0	[erg s^{-1}]	5.5×10^{38}	9.5×10^{38}	3.5×10^{38}	7.2×10^{38}
	Max. Eff.$_X$	...	1917.2	46.3	3.7	45.3
	t(max.eff)$_X$	[years]	7750.0	5700.0	6850.0	11750.0
	Dos$_X$	[years]	450.8	690.6	523.8	1332.2
	$t_{\rm start-X}$	[years]	7333.2	5159.4	6526.2	10717.8
	$t_{\rm end-X}$	[years]	7784.0	5850.0	7050.0	12050.0
	Dor	[years]	1155.7	1857.5	2910.4	5193.0
	$t_{\rm start-R}$	[years]	6644.0	4105.0	4686.0	7313.0
	$t_{\rm end-R}$	[years]	7799.7	5962.5	7596.4	12506.0
model 5	L_0	[erg s^{-1}]	1.7×10^{38}	3.0×10^{38}	1.1×10^{38}	2.0×10^{38}
	Max. Eff.$_X$	...	5444.4	325.6	54.2	886.0
	t(max.eff)$_X$	[years]	8336.5	5850.0	6910.0	11350.0
	Dos$_X$	[years]	323.6	408.8	360.0	584.4
	$t_{\rm start-X}$	[years]	8042.9	5521.5	6616.6	10846.1
	$t_{\rm end-X}$	[years]	8366.5	5930.3	6976.6	11430.5
	Dor	[years]	1036.9	1289.3	1702.9	2960.9
	$t_{\rm start-R}$	[years]	7337.0	4676.0	5342.0	8526.0
	$t_{\rm end-R}$	[years]	8373.9	5965.3	7044.9	11486.9

Table 4.2: Table 1, continued.

anchor PWN:			J1834.9-0846	Crab	G0.9+0.1	G54.1+0.3
model 6	L_0	[erg s^{-1}]	5.5×10^{37}	9.5×10^{37}	3.5×10^{37}	7.2×10^{37}
	Max. Eff.$_X$	...	12507.8	1950.9	393.3	5464.0
	t(max.eff)$_X$	[years]	8854.2	6272.1	7297.3	11812.3
	Dos$_X$	[years]	231.6	271.2	235.2	348.4
	$t_{\rm start-X}$	[years]	8640.6	6020.9	7087.1	11493.9
	$t_{\rm end-X}$	[years]	8872.3	6292.1	7322.3	11842.3
	Dor	[years]	931.4	1025.9	1284.8	2241.6
	$t_{\rm start-R}$	[years]	7947.0	5281.0	6059.0	9620.0
	$t_{\rm end-R}$	[years]	8878.4	6306.9	7343.8	11861.6
model 7	L_0	[erg s^{-1}]	1.7×10^{37}	3.0×10^{37}	1.1×10^{37}	2.0×10^{37}
	Max. Eff.$_X$	...	26368.0	7230.6	1956.5	24111.6
	t(max.eff)$_X$	[years]	9270.0	6739.3	7844.7	12799.8
	Dos$_X$	[years]	157.6	198.9	171.0	217.7
	$t_{\rm start-X}$	[years]	9123.3	6555.4	7693.7	12600.9
	$t_{\rm end-X}$	[years]	9281.0	6754.3	7864.7	12818.6
	Dor	[years]	812.6	901.4	1100.4	1843.3
	$t_{\rm start-R}$	[years]	8472.0	5861.0	6774.0	10984.0
	$t_{\rm end-R}$	[years]	9284.6	6762.4	7874.4	12827.3
model 8	L_0	[erg s^{-1}]	5.5×10^{36}	9.5×10^{36}	3.5×10^{36}	7.2×10^{36}
	Max. Eff.$_X$	...	50724.6	17457.5	6530.7	57685.8
	t(max.eff)$_X$	[years]	9599.4	7194.8	8394.8	13645.4
	Dos$_X$	[years]	106.0	150.9	142.7	167.4
	$t_{\rm start-X}$	[years]	9499.0	7052.4	8263.8	13487.4
	$t_{\rm end-X}$	[years]	9604.9	7203.3	8406.5	13654.9
	Dor	[years]	688.8	813.1	987.3	1667.2
	$t_{\rm start-R}$	[years]	8918.0	6395.0	7426.0	11993.0
	$t_{\rm end-R}$	[years]	9606.8	7208.1	8413.3	13660.2
model 9	L_0	[erg s^{-1}]	1.7×10^{36}	3.0×10^{36}	1.1×10^{36}	2.0×10^{36}
	Max. Eff.$_X$	...	94499.4	40631.0	18523.9	145837.0
	t(max.eff)$_X$	[years]	9859.3	7567.8	8870.1	14560.2
	Dos$_X$	[years]	68.7	124.7	116.0	115.7
	$t_{\rm start-X}$	[years]	9794.2	7454.5	8760.8	14450.4
	$t_{\rm end-X}$	[years]	9862.8	7579.1	8876.8	14566.2
	Dor	[years]	568.1	717.4	871.8	1454.3
	$t_{\rm start-R}$	[years]	9296.0	6862.0	8009.0	13115.0
	$t_{\rm end-R}$	[years]	9864.1	7579.4	8880.8	14569.3
model 10	L_0	[erg s^{-1}]	5.5×10^{35}	9.5×10^{35}	3.5×10^{35}	7.2×10^{35}
	Max. Eff.$_X$	...	166724.6	96896.9	50159.2	293947.0
	t(max.eff)$_X$	[years]	10070.4	7871.0	9241.3	15141.3
	Dos$_X$	[years]	62.7	77.2	93.4	94.8
	$t_{\rm start-X}$	[years]	10010.0	7800.1	9153.2	15051.6
	$t_{\rm end-X}$	[years]	10072.7	7877.2	9246.6	15146.3
	Dor	[years]	459.0	608.4	744.8	1259.9
	$t_{\rm start-R}$	[years]	9614.0	7269.0	8504.0	13888.0
	$t_{\rm end-R}$	[years]	10073.0	7877.4	9248.8	15147.9

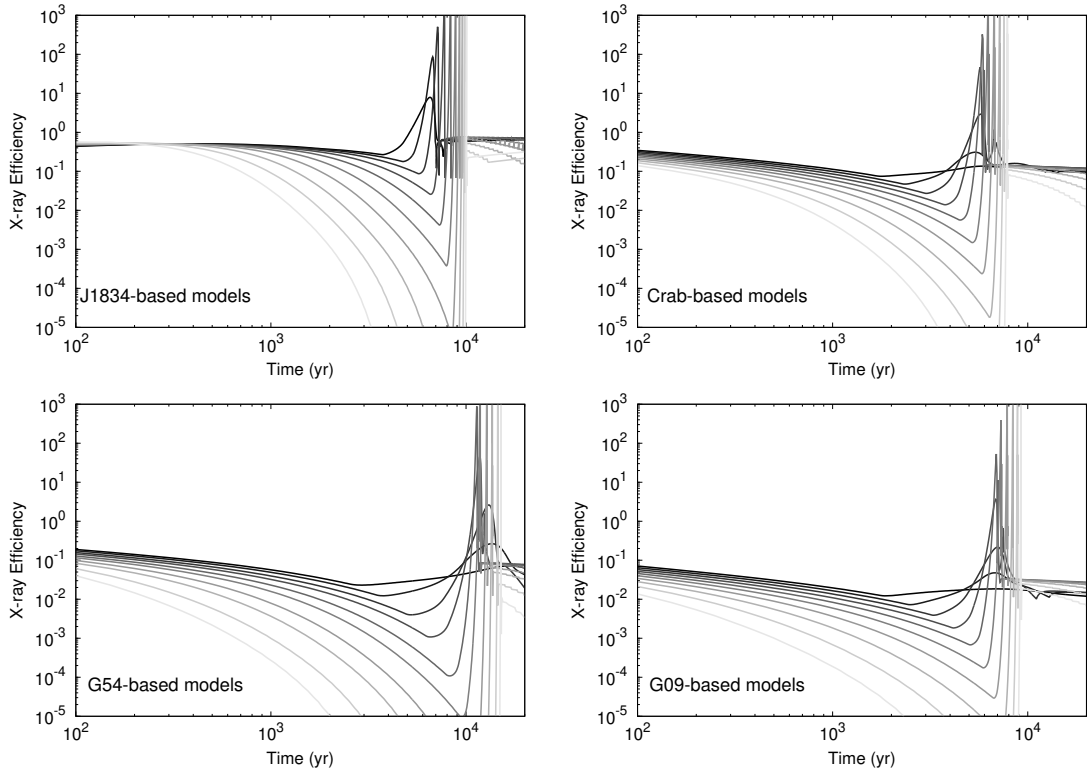

Figure 4.2: The evolution of X-ray efficiency for all models studied. The four panels correspond to each of the four anchor-PWNe analyzed. In each panel, the different grey levels are used to show the 10 corresponding models, with the lightest color representing the model with the lowest L_0, as in Fig. 4.1.

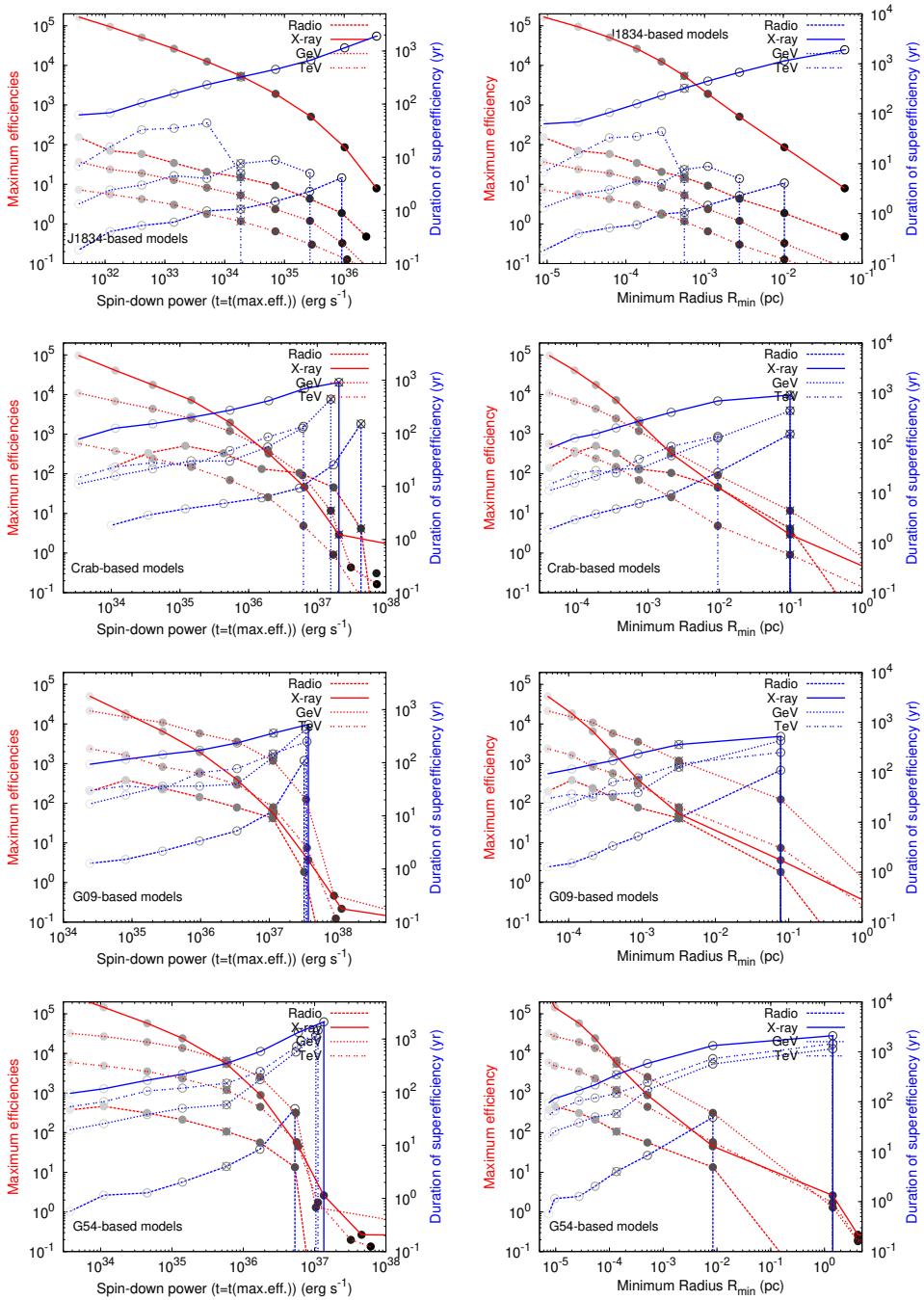

Figure 4.3: Exploring the superefficiency phase space. See text for a discussion.

spin-down power. Maximum efficiencies are shown by the red lines, corresponding to the left vertical axis, while the duration of the superefficiency periods are shown by blue lines, referenced to the right vertical axis. Different type of lines denote different energy bands.

The values of $t(\text{max.eff})_X$ referred in Table 1 represent the time it takes (since its birth) to the putative PWN in reaching its maximum X-ray efficiency level. The latter is defined as the ratio between the X-ray luminosity and the spin-down power, which is a function of time. The $t(\text{max.eff})_X$ time interval is also depicted in the corresponding Fig. 4.1 panel with a line representing the evolution since birth ($L_{sd} = L_0$) up to that moment. Whether that maximum efficiency happens 'today' (i.e., approximately at the time the dots representing ATNF pulsars in Fig. 4.1 are plotted) depends of course on the real time of birth of such putative pulsars.

The panels of Fig. 4.3 show the maximum efficiency in different bands and the corresponding duration of the superefficiency interval as a function of the spin-down power at the time at which the corresponding maximum efficiency is reached (left), and of the minimum radius that is attained (right). Each panel refers to a given set of PWNe constructed using the same anchor system, as referred to in the plot. As described above, models within each panel all are subject to the same environment. Also, for a given pulsar, the spin-down power is assumed to be uniformly decreasing with time as per the set of equations above, and all sets of models assume the same approximate range of initial spin-down powers as given in Table 1. This is color-coded in the dots representing the models within Fig. 4.3, with the lightest color assigned to the smallest initial spin-down power.

Within the same panel, the maximum efficiencies happen at different ages of the PWN, because the underlying models have different energetics, and thus the studied PWNe have different rotational power when the nebula reaches the maximum efficiency. From one set of models (one panel) to another, the assumed pulsar properties and environment also change, contributing to additional differences due to their different pulsar evolution, e.g., because of having a different braking index and being subject to a different medium feedback. Models with larger braking index and smaller age have larger spin-down power at $t = t(\text{max.eff})$.

The left panels of Fig. 4.3 show that for PWNe evolving in a similar environment, the maximum efficiencies are uniformly decreasing with the spin-down power, whereas the duration of the process is longer. When the central energy is larger and the pulsar is more powerful, there is a larger pressure in the PWNe they generate, better supporting the environmental feedback. As a result, the compression is smaller and lasts a longer time. Radio, GeV and TeV superefficiency may appear as well, but not for sufficiently energetic pulsars. For instance, for J1834-based models, there is no superefficiency at high energies as soon as the pulsars' spin-down power at the time of the maximum exceeds $\sim 2 \times 10^{35}$

and $\sim 2 \times 10^{34}$ erg s^{-1} for superefficiency at the GeV and TeV bands, respectively. Equivalently, there is no superefficiency at the GeV and TeV bands as soon as L_0 exceeds $\sim 5.5 \times 10^{37}$ erg s^{-1} and $\sim 5.5 \times 10^{36}$ erg s^{-1}, respectively. For the third set of models, based on G09, superefficiency in all the 4 bands disappears when the spin-down power at $t = t(\text{max.eff})$ exceeds $\sim 2 \times 10^{37}$ erg s^{-1}, or when L_0 exceeds $\sim 3.5 \times 10^{37}$ erg s^{-1}.

The right panels of Fig. 4.3 show that the minimum radius attained is (correspondingly) smaller for the more efficient nebulae. The minimum radius can reach in extreme models values as small as just a few times 10^{-5} pc, albeit this is not the common case. However, although small, and as we noted earlier, even the more extreme cases produce PWNe that are orders of magnitude larger than the pulsar's magnetosphere (typically at least 5 orders of magnitude larger than the size of a young pulsar's light cylinder), and pulsed emission via synchro-curvature radiation (e.g., see Torres 2018) is not expected to be affected.

The crosses in all curves of each panel of Fig. 4.3 show the properties of the superefficiency period of the real PWN. When, for instance, J1834 reaches the maximum X-ray efficiency, the spin-down power will be of the order of 2×10^{34} erg s^{-1}, not far from its current value, being the X-ray maximum just a few hundreds years ahead. There are small differences as to when the maximum at other energy ranges happens in comparison with that in X-rays, what is reflected -albeit difficult to see in this scale at times- in Fig. 4.3.

Both the maximum efficiency and duration of the X-ray and radio superefficiency period (and every other frequency in between) are typically larger than those corresponding to higher-energy bands, what is especially notorious in the J1834-based models. The physical reasons why this happens were discussed in detail before. From this perspective, then, searches in radio, optical or X-rays are likely to be more relevant than in gamma-rays. Additionally, given that the angular resolution of lower-frequency instruments is better in comparison with gamma-ray ones, it seems that these frequencies are naturally preferred for a search. Despite this fact, higher-energy instruments able to do unbiased surveys (e.g., using *Fermi*-LAT or the Galactic survey of H.E.S.S. or CTA) may uncover good candidates.

We note that less superefficient PWNe, with maximum X-ray efficiencies in the range of a few hundreds, or a few tens, will have a larger probability to be found in comparison to PWNe having more extreme reverberation episodes, given that they spend a longer fraction of their life in this period. For pulsars of small spin-down power (from 10^{32} to a few times 10^{34} erg s^{-1}) the X-ray maximum efficiency can be at least a factor of 1000 larger than the spin-down power at the time. For instance, taking the models based on J1834 as example, the model 9 has one of the largest X-ray efficiency of all, reaching $\sim 9 \times 10^4$, which implies a luminosity $L_X \sim 10^{37}$ erg s^{-1} at that time. However, the superefficient period as a whole is active only for 68 years, and only for 16 years the X-ray efficiency is larger than 10^3 ($L_X \sim 10^{35}$ erg s^{-1}). J1834 itself, with a current spin-down

power $L_{sd} \sim 1.87 \times 10^{34}$ erg s^{-1} and a future maximum superefficiency of 5444 will have a peak X-ray luminosity $L_X \sim 10^{38}$ erg s^{-1}. The period of X-ray superefficiency lasts in this case for 316 years, and the period for efficiency larger than 1000 would only be ~ 60 years. Less superefficient PWNe such as the J1834-based model 1 and others alike, with maximum X-ray efficiency of ~ 8, may have a larger probability to be found, given that the period of interest lasts 1900 years. In any case, these are strong but short events in the life of stars, and will clearly be difficult to find.

4.2.4 How many superefficient PWNe are there in the Galaxy?

In our initial work, we roughly estimated that there could not be more than a few PWNe in an active superefficient stage today (or at any given time) in the Galaxy. Given that the superefficiency period of the real PWNe studied in the previous chatper lasted a few hundreds years, we were interested in $\sim$3% of the evolution of the pulsars born in the last ten millennia. Thus, given the pulsar birth rate, we would not expect more than a few Galactic nebulae to be currently superefficient.

In the framework of our specific radiative/dynamical model, one can obtain a more specific assessment. Since we now have many PWNe models studied in detail, and that for each of them we know when (with respect to the pulsar birth) and for how long their superefficiency stage happens, we can improve the reliability of our earlier estimate. To do so we shall assume the birthrate of pulsars in the Galaxy is 2.8 per century, as determined by Faucher et al. (2006). We shall randomly associate to each member of a set of 500 pulsars (the number of pulsars appearing in the Galaxy in the last 17800 years, according to the birth rate) a given value of initial magnetic field and period. We shall do so in a way that is compatible with the results obtained in population synthesis models of isolated neutron stars with magneto-rotational evolution (Gullon et al. 2014). Thus, we shall consider that the logarithm of the initial magnetic field (in Gauss) with which pulsars are born is described by a Gaussian with mean of 13 and a standard deviation of 0.6; and that the initial period distribution is uniform for values less than 0.5 seconds. With these assumptions, and the fact that the magnetic field is described as usual by $B(t) = 6.4 \times 10^{19}\sqrt{P(t)\dot{P}(t)/\text{s}}$ G, (i.e., under the assumption of magnetic dipole domination of the Poynting flux, see Petri (2015) the distribution of initial spin-down powers is fixed using Eq. 4.4; since $L_{sd} \propto B^2/P^4$. Fig. 4.4 shows an example of the resulting distribution of initial magnetic fields, periods, and spin-down powers for a simulated set of the youngest 500 pulsars born in the Galaxy that is compatible with population synthesis models. In order to obtain averaged results, we repeat this random assignment of initial pulsar properties, generating 5000 different sets (further runs do not change the results) of 500 pulsars, always agreeing with population synthesis models. For each pulsar in a simulated set, we thus know its age (the randomly assigned t_{birth} according to the

pulsar birth rate assumed) and its energetics. If the initial spin-down power is within the range explored in Table 1, we consider the closest L_0-values among the cases studied there to represent the PWN evolution. If so, we know that the PWN will be in a superefficient stage today if $t_{\rm start-X} < t_{birth} < t_{\rm end-X}$, where $t_{\rm start-X}$ and $t_{\rm end-X}$ are the initial and final times for the X-ray superefficient period. Of course, $t_{\rm end-X} - t_{\rm start-X} = {\rm Dos_X}$. Specific values are given in Table 1. If the initial spin-down power of the simulated pulsar is off the range of simulated models in Table 1 (either from below or from above) we shall consider that no superefficiency happens. More luminous pulsars continue the trend of decreasing maximum efficiency shown in Fig. 4.3, and indeed no superefficiency happens. These pulsars are in any case unlikely to appear, being in the tail of the distribution of L_0. Less luminous pulsars than those in Table 1 may have superefficient events, but are so short in duration that in practice they also contribute little or nothing to the total expected number.

On average after 5000 simulated sets, we find that out of the last 500 pulsars born in our Galaxy, simulated according to population synthesis results, 308.7 $\pm$ 11.0 of them are assigned an L_0 value within the range explored in Table 1. And out of them, the mean number of superefficient PWNe is 1.8 $\pm$ 1.3. The last panel of Fig. 4.4 shows the histogram density for the number of superefficient PWNe out of the 5000 simulations. At any given time in the Galaxy, then, our results imply that typically between 0 and 3 PWNe should be in a superefficient stage.

4.2.5 How many reverberating PWNe are there in the Galaxy?

Using the same approach, we can calculate as well how many PWNe are currently in a reverberation stage. Particularly, how many of them are actually contracting. Here, however, given that we have detailed models only for a range (although broad) of L_0, and that reverberation could also happen for pulsars having initial spin down powers out of this range, our average should be considered a lower limit. Less luminous pulsars than those in Table 1 have in any case shorter reverberation periods as a whole, of a few hundred years at most, and missing them completely in our calculation is not expected to affect our average significantly. We find that out of the youngest 500 pulsars born in our Galaxy, those having L_0 values between $\sim 10^{35}$ and $\sim 10^{40}$ erg s^{-1}, would lead to 16.7$\pm$3.8 currently contracting PWNe. This is a relatively large number that promotes observational searches.

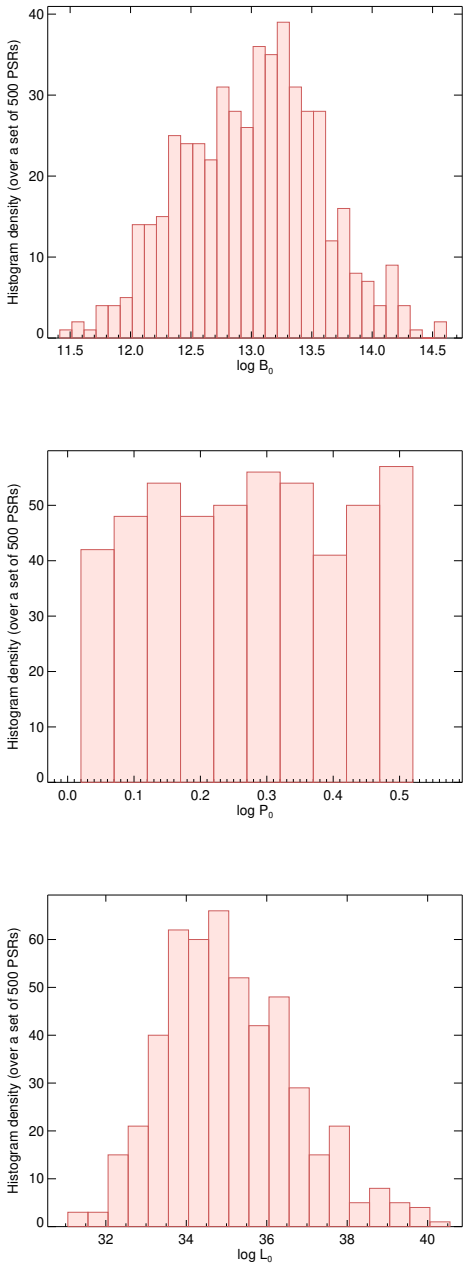

Figure 4.4: Example of the random distributions of B_0, P_0, and L_0 considered for a set of 500 pulsars.

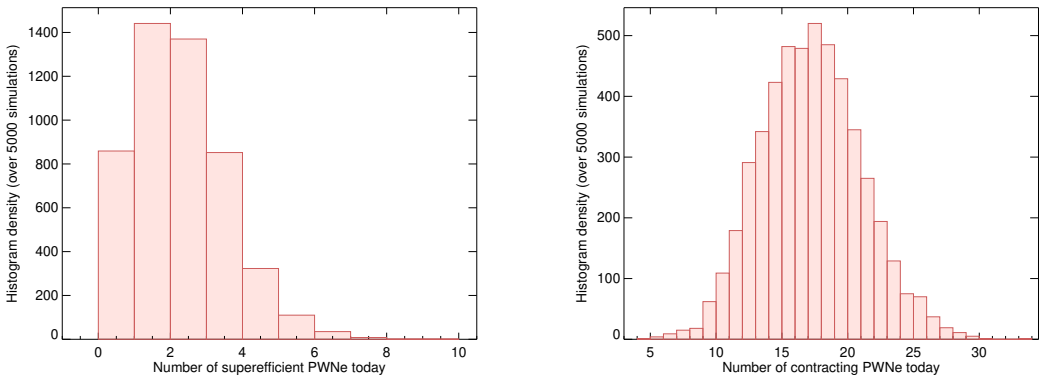

Figure 4.5: Histogram density of the resulting number of Galactic PWNe that are superefficient and contracting today.

4.3 Observational search of superefficient PWNe

4.3.1 May we have detected a superefficient PWN candidate already?

Probably not. Since all X-ray sources in the Galaxy with luminosity $L_X > 1 \times 10^{35}$ erg s^{-1} have been already identified (e.g., Van den Berg (2012)), we can safely conclude that if any PWN is currently in a superefficient stage, it must be a relatively dim system. However, out of the models studied, we do not find clear cases of PWNe for which the spin-down power at the time of the maximum efficiency is $< 10^{34}$ erg s^{-1} and the X-ray superefficiency is < 10. We thus conclude that observing PWNe not in superefficiency, but on the path towards superefficiency may be a better approach to test our theoretical predictions (see the next Section). Before tackling this, we shall first confront our prejudice and look for any possible superefficient PWN candidate in archival data.

Based on our theoretical computations, we hunted for superefficient PWNe candidates that may have already been detected adopting three different approaches. As a first check, promising candidates were selected by cross-matching young ($\tau_c \lesssim 10$ kyr) pulsars with a relatively low spin-down power ($L_{sd} \lesssim 10^{34}$ erg s^{-1}) listed in the ATNF pulsar catalog (v. 1.59; see Manchester et al. 2005) with unidentified point-like sources listed in the *XMM-Newton* slew survey catalog Saxton et al. (2008) that might be associated with bright X-ray emission from the putative surrounding PWN. We did not find any pulsar fulfilling all the requisites above besides the known magnetars, high-magnetic-field pulsars and central compact objects.

Note that TEX he *XMM-Newton* slew survey covers about 84% of the whole sky with a sensitivity limit on the observed flux of $\sim 1.2 \times 10^{-12}$ erg cm^{-2} s^{-1} in the 0.2–12 keV

Table 4.3: Multiwavelength properties of the two sources selected as possible superefficient PWNe candidates in the *XMM-Newton* slew survey catalog, and detected in our recent *Swift* observations (see the text for details). Luminosity is in units of (10^{31} erg s^{-1}).

Source name	R.A., Decl. (J2000.0)	D (pc)	XRT cr (counts ks^{-1})	$N_{\rm H}$ (10^{21} cm^{-2})	Γ	L_X	*Gaia* mag	UVW2 mag
J123629.8−664549	$12^h36^m32^s.59$, -66°46'01".6	362	120 ± 10	3.7 ± 1.5	1.5 ± 0.3	14 ± 2	17.7	18.24 ± 0.09
J194402.0+284451	$19^h44^m01^s.90$, +28°44'51".6	434	97 ± 11	1.0 ± 0.9	1.8 ± 0.5	9 ± 1	17.6	16.56 ± 0.05

energy interval.

Alternatively, bright PWNe could exist around particularly faint radio pulsars which might have not been detected yet by means of radio pulsar surveys (and hence are not listed in the ATNF catalog). We thus searched for unidentified X-ray sources at low Galactic latitude ($|b| < 4°$) listed in the *XMM-Newton* slew survey catalog with a flux $F_X > 10^{-11}$ erg cm^{-2} s^{-1} over the 0.2–12 keV energy band, and never observed using dedicated X-ray pointings.

Notably, this criterion selects only three sources, XMMSL2 J180205.6−251231 (at $b = -1.3°$), XMMSL2 J123629.8−664549 (at $b = -3.9°$) and XMMSL2 J194402.0+284451 (at $b = 2.4°$). We requested follow-up X-ray and UV observations with the *The Neil Gehrels Swift Observatory* (Gehrels et al. 2004) for these sources, and the results are as follows.

J180205.6−251231 was not detected by the X-ray Telescope (XRT) during our 1-ks observation on 2018 May 20 (observation ID: 010693001). We set a 3σ upper limit of 0.01 counts s^{-1} on the background-subtracted count rate over the 0.3–10 keV energy range at the position quoted in the *XMM-Newton* slew catalog. This rules it out as a PWN candidate in a superefficient phase. The *Swift* observation of J123629.8−664549 started on 2018 May 23 at 06:08:53 (UTC) and lasted 1.1 ks (obs. ID 0001069400). That of J194402.0+284451 started on 2018 May 31 at 12:29:42 (UTC) and lasted 0.8 ks (obs. ID 00010695002). In both observations, the XRT was operated in the photon counting mode, and the Ultraviolet and Optical Telescope (UVOT) in image mode using the UVW2 filter. The two sources were detected by both the XRT and the UVOT, and are also spatially coincident with sources in the *Gaia* release (Gaia 2018). From these findings, we can infer their distances as well as the presence of a relatively bright UV/optical counterpart. Table 2 reports a summary of their properties. Coordinates are taken from the second *Gaia* data release (Gaia 2018). Distances were computed from the parallaxes measured with *Gaia* using a Bayesian method with exponentially decreasing volume density prior and accounting for the known systematic zero-point offset of -29 μas in the *Gaia* parallaxes. The 16th and 84th percentiles are reported

in parentheses (see Bailer-Jones et al. 2018 for details). The XRT count rates and the X-ray luminosities refer to the 0.3–10 keV energy range. Optical magnitudes are evaluated over the 3300–10500 Å wavelength range. All quoted magnitudes are not corrected for absorption, and uncertainties on the UV values are quoted at a confidence level of 1σ. We rule out that these sources could be good superefficient PWNe candidates owing to their low X-ray luminosity.

Finally, as a third search approach, we consider that our model predicts that the superefficient radiation mechanism may often yield to detectable gamma-ray emission (see Fig. 4.3). However, on the one hand, cross-correlation between sources in the *XMM-Newton* slew survey catalog and unidentified TeV sources listed in the *H.E.S.S.* survey of the Galactic plane (HESS Galactic Plane Survey, published in 2018) did not yield any match. On the other hand, we found a few X-ray bright sources in the *XMM-Newton* slew catalog (with $F_X > 10^{-11}$ erg cm^{-2} s^{-1} in the 0.2–12 keV energy band) positionally coincident with unidentified gamma-ray sources listed in the preliminary *Fermi* Large Area Telescope (LAT) eight-year point source list.[1] However, the location of these sources are well above the Galactic plane ($|b| > 10^\circ$ for all of them), and are thus probably not related to any Galactic object. The deep all-sky X-ray survey that will be performed with the upcoming mission *e-ROSITA* (Merloni et al. 2012) is expected to lead to the discovery of several new fainter unidentified X-ray sources along the Galactic plane. Such a survey, coupled to the continuous monitoring of the Galactic plane in the GeV-TeV domain with *Fermi* LAT and *H.E.S.S.*, will increase the chance to detect (fainter) Galactic superefficient PWNe candidates based on the above-mentioned criteria.

4.4 Observational search of reverberating PWNe

4.4.1 Observing reverberating PWNe

Given how unlikely it is that we have already detected a superefficient PWN, as well as because of the larger number of PWNe that are expected to be in the reverberation phase now, it makes sense to search for observational signals of the latter. When identified, these PWNe will be running on the path towards their maximum efficiency, which will be expected to happen relatively soon (maybe just a few hundred years ahead). Although the rate of change of observational features such as flux and spectrum may not be as large as it is in the superefficient phase, reverberating PWNe models provide predictions that might be at reach for current and/or forthcoming telescopes.

Probably the best candidate for this study is the recently detected PWN around the magnetar J1834.9-0846 (Younes et al. 2012, Younes et al. 2016). We have modelled this PWN in the same framework we are using in this work before Torres (2017), as

[1] *https://fermi.gsfc.nasa.gov/ssc/data/access/lat/fl8y/*

well as provided a detailed discussion regarding the dynamical situation, its age, and its birth supernova. We concluded there that this PWN can be rotationally-powered, despite having the largest efficiency known in X-rays, if it has recently entered into its reverberation phase. The deduced age today, 7970 years, is consistent with other dynamical features of the systems, its (non-)relation with W44, and the general energetics. We pose here that if J1834 is indeed reverberating, some changes in the following 50 years should be detectable. We start by describing them in Fig. 4.6. The upper panel of that figure represents the SED at the current time, whereas the lower panel represents the time evolution of this SED as it will look 50 years into the future, so as to give a rough, preliminary idea of the changes expected. Both the model and the origin of the (current) data set used for a comparison are detailed in Torres (2017), from where the model parameters were taken. Briefly, the GeV data comes from Li et al. (2017) analysis of 6-years of *Fermi*-LAT data of observations of all magnetars, including J1834. Having removed the surrounding gamma-ray sources, and modelled out W41, the upper limits apply to the nebula directly. The TeV data represent the spatially coincident source HESS J1834-087 (Aharonian et al. 2006, Albert et al. 2006), which may be unrelated to the PWN J1834, but originated in the interaction of particles accelerated in the W41 SNR with molecular clouds in the vicinity, e.g., (Aharonian et al. 2006, Albert et al. 2006, Tian et al. 2007, Li et al. 2012, Castro et al. 2013, Abramowski et al. 2015), similar to the case of W44 (Uchiyama et al. 2012), or W28 (Hanabata et al. 2014). Thus, we shall consider the TeV data from HESS J1834-87 to represent upper limits to the putative TeV emission of the magnetar nebula. The photon energy density in the infrared and far-infrared are assumed such that the model would produce the maximum TeV emission still in agreement with these observations. For further details on the data used and the model itself see Torres (2017).

The flux given in the plot of Fig. 4.6 is obtained just as distance-diluted luminosity predictions, so that possible effects along propagation (e.g., absorption in the optical or UV) are not considered. It is clear that J1834.9-0846 will become visibly brighter 50 years from now than what currently is. The heating of electrons produced by the compression of the PWN is the reason behind this behavior. This is shown in Fig. 4.7 where the color scale shows the time evolution of both electrons and losses, in steps of 5 years. Differences are almost imperceptible in this scale, except for the region of the maxima, where the burning is more extreme as time goes by.

The two upper panels of Fig. 4.8 show the subsequent evolution of the PWN in context. The first panel shows the evolution of the radius and the enhancement of the magnetic field due to the reverberation process. The top-left panel shows an extended period of time covering the whole process of contraction and re-expansion. The grey-shaded region zooms in a period of 50 years starting in 2017. The magnetic field

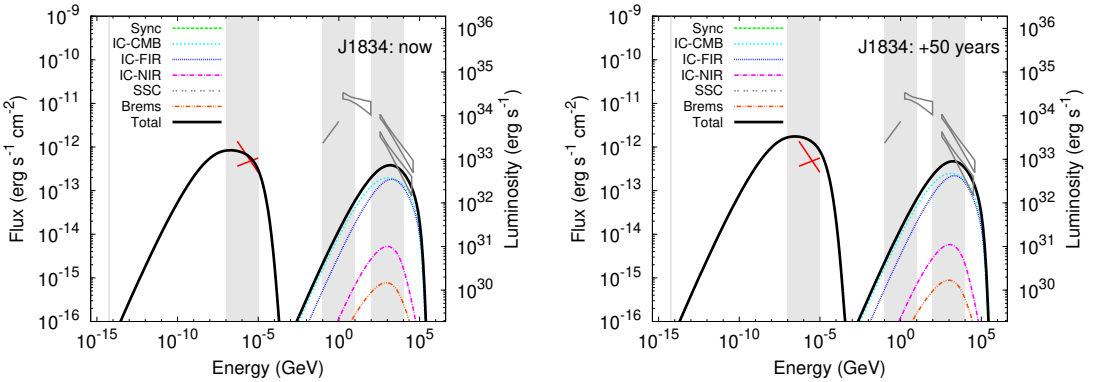

Figure 4.6: Spectra of the nebula J1834 now and in 50 years from now. The data is the same in both cases, and although not simultaneous they are obviously closer to the current time, so that in the second panel are put only for reference. See text for discussion. The grey vertical lines and 3 grey rectangles from left to right represent the energy ranges considered for radio, X-ray, GeV and TeV, although data in the latter two ranges are only considered as upper limits –and the model parameters are thus taken to match them only to give a constraint on photon densities.

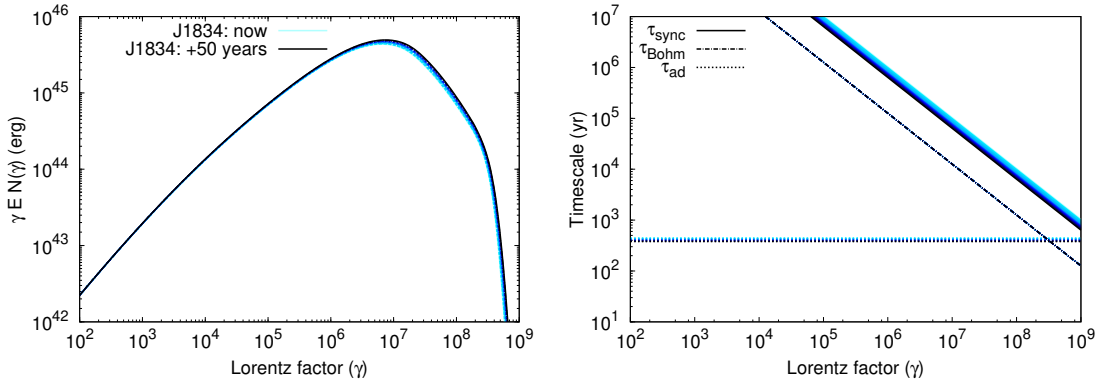

Figure 4.7: Evolution of the electron spectrum as well as the timescales of electron losses via synchrotron radiation, Bohm diffusion, and the adiabatic gain of energy due to the contraction of the system. The color scale (from light to dark, the same used in the next figures) shows the time evolution, in steps of 5 years, although curves are close in this scale to individually distinguish them.

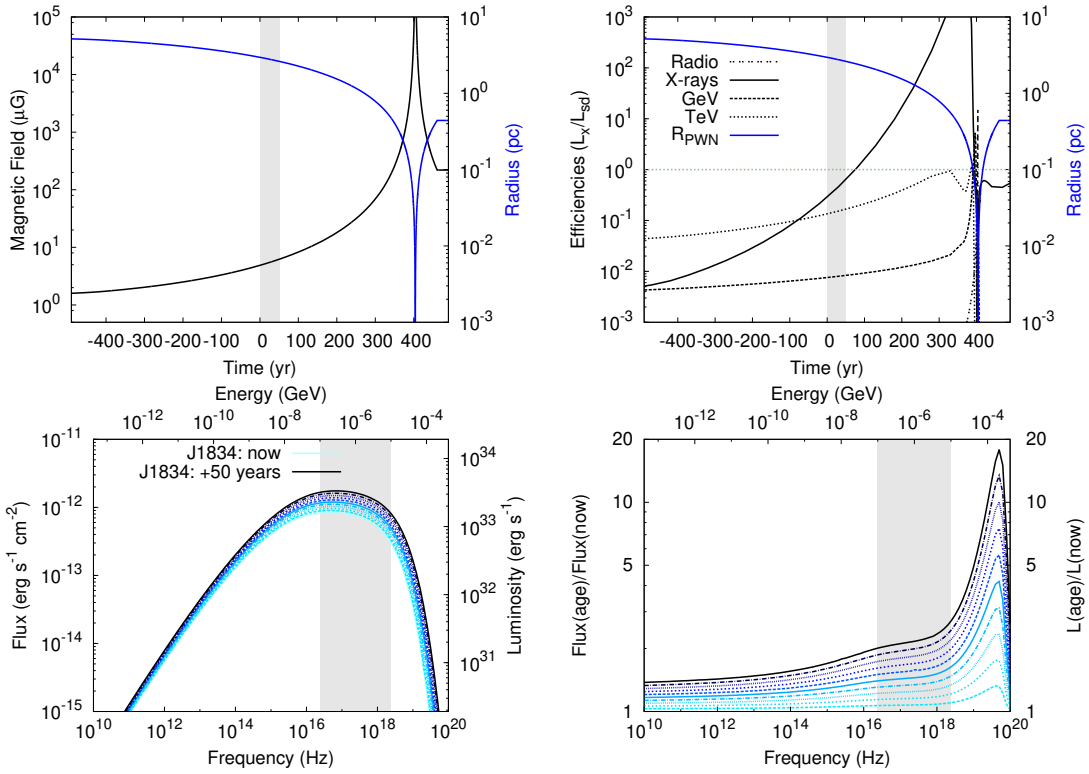

Figure 4.8: Top: Contraction and enhancement of the magnetic field due to reverberation process. The label 0 in the x-axis represent the current time, with positive (negative) values following the evolution towards the future (past). The top-right panel shows the evolution of the efficiencies of the emission along time. The grey shadows in the top panels represent the sub-sequent 50 years of evolution. The bottom plots emphasizes the changes expected in the X-ray spectra. The grey shadows in the bottom panels show the region of 0.1–10 keV.

and radius of the nebula increases and decreases, respectively, as a shallow power law in this period, both with variations well within a factor of 2. The top-right panel shows the evolution of the efficiency. It is clear that despite the minimal changes in radius and magnetic field described above, the X-ray efficiency (and luminosity) is the most affected, also reaching a change up to a factor of 2 within the next 50 years. This is better seen in the evolution of the synchrotron spectrum and in the evolution of the ratio of luminosities (bottom panels) normalized to the one attained today, and with the same color coding in steps of 5 years. From the last panel we also see that the harder the X-ray energies of the measurement, the better, since the synchrotron emission is more affected at the largest electron energies.

4.4.2 Are the changes predicted for the J1834 PWN observable?

Our model makes specific predictions on the time evolution of the X-ray emission properties of the nebula around J1834, which can be tested against observations. As an illustrative case, we verified if the expected flux increase of the nebula could be detectable with the *XMM-Newton* EPIC pn instrument (Struder et al. 2001) over a timescale of 10 yrs between the epoch of the last observations in 2014 (Younes et al 2016) and 2024. We assumed an uncertainty of 10% on each data point in the theoretically predicted SEDs of the nebula at the two epochs, and fitted a power law model to the data points over the 0.3–10 keV energy range. This allowed us to estimate the expected photon index and the intrinsic (i.e. unabsorbed) flux of the nebula at the two epochs. We note that assuming a slightly smaller and/or larger uncertainty on the SED data points yielded values for the photon index and the flux fully consistent with each other. On the one hand, the SEDs show no substantial change in the spectral slope, in agreement with what was found by Younes et al. (2016) when comparing with earlier observations. On the other hand, they imply a flux increase of $\Delta F_X \simeq 4 \times 10^{-13}$ erg cm^{-2} s^{-1} between 2014 and 2024.

We carried out simulations using the FAKEIT tool within XSPEC. We assumed for simplicity no dependence of the spectral shape of the nebula on the location, i.e. we considered the case of a homogenous emitting nebula. We accounted for the absorption by neutral interstellar material along the line of sight adopting the value for the hydrogen column density reported by Younes et al. (2016) assuming the photoionization cross-sections from (Verner 1996) and the chemical abundances from (Wilms et al. 2000), i.e. $N_{\rm H} = 8 \times 10^{22}$ cm^{-2}. We used the latest versions of the response files for the pn in the extended full-frame configuration and with medium optical blocking filter in place (i.e. the same setup adopted in 2014). Background spectra were extracted from the pn data acquired in 2014 using the same prescriptions outlined by Younes et al. (2016). We simulated a 130 ks-spectrum for the 2014 epoch. This corresponds to the effective net exposure time of the *XMM-Newton* EPIC pn observations at the same epoch (see table 1 by Younes et

Table 4.4: Predicted time evolution of the nebula unabsorbed flux over the 0.3–10 keV energy band, and results of our simulations with *eXTP* and *Athena*. 1σ uncertainties are reported on the fluxes measurable at the different epochs with 100-ks exposures (see the text for details).

Year	Predicted flux (10^{-12} erg cm^{-2} s^{-1})	Instrument	Measurable flux (10^{-12} erg cm^{-2} s^{-1})
2024	2.69	*eXTP* SFA	2.67 ± 0.04
2027	2.82		2.79 ± 0.04
2030	2.95	*Athena* WFI	2.92 ± 0.03
2033	3.10		3.09 ± 0.03

al. 2016). Different exposure times were adopted instead to simulate the spectrum as would be acquired in 2024. We then modelled each spectrum with an absorbed power law, holding $N_{\rm H}$ fixed to the above-mentioned value, and allowing the photon index and the normalization to vary.

Spectral fitting as a function of time shows that an 80-ks exposure with the EPIC pn in 2024 would allow us to measure the X-ray flux of the nebula with enough accuracy to detect the predicted flux increase on a 10 yr-timescale at a confidence level $\gtrsim 4\sigma$. This measurement would be more precise (or done in a shorter time) if observed with more sensitive instruments than EPIC pn. Such a relatively short observation would confirm the PWN is indeed reverberating, and open the gate to testing particular details of the model.

In particular, to test whether the predicted rate of flux increase could be detected on timescales as short as three years with future X-ray imaging instruments, we simulated the spectra of the nebula as would be acquired by the Wide Field Imager (henceforth WFI; Meidinger et al. 2017) on board the *Advanced Telescope for High Energy Astrophysics* (*Athena*), as well as by the Spectroscopic Focusing Array (SFA; Zand et al 2019) on board the *enhanced X-ray Timing and Polarimetry mission* (*eXTP*), following the procedure outlined above. The fluxes expected at four different epochs over the planned mission durations (2023–2028 for *eXTP* and 2028–2033 for *Athena*) are listed in the second column of Table 4.4. Our simulations are aimed at detecting the rate in the flux increase predicted by our models, $\simeq (4-5) \times 10^{-14}$ erg cm^{-2} s^{-1} yr^{-1} on a timescale of 3 years between 2024 and 2033.

We employed the latest versions (2017 November) of the response files for the nominal WFI mirror configuration with 19 rows and without external light blocking filter. We also accounted for the expected instrumental and diffuse background level using the publicly available, latest version (2018 July) of the background files for extended sources[2].

[2] *http://www.mpe.mpg.de/ATHENA-WFI/response_matrices.html*

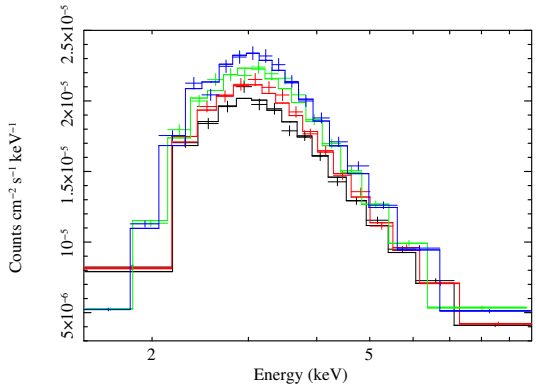

Figure 4.9: Simulated spectra of J1834's nebula at four different epochs (see the text for details). Black: in 2024; red: in 2027; green: in 2030; blue: in 2033. For plotting purpose, spectra have been rebinned and are shown over the 1.5–10 keV energy range.

Similarly, we adopted the latest versions of the response, auxiliary and background files to simulate the spectra related to the SFA [3]. Spectral fitting as a function of time shows that 100-ks effective exposures would allow us to measure the X-ray flux of the nebula with enough accuracy to detect the predicted flux increase on a 3 yr-timescale at a confidence level $\gtrsim 3\sigma$ (see Table 4.4). The simulated spectra at the different epochs are shown in Figure 4.9.

4.5 Concluding remarks

We have studied, from both a theoretical and an observational perspective, reverberating and superefficient PWNe. Based on a series of systematically studied PWNe models we quantified the duration and significance of these periods in the PWN evolution. Our theoretical results for the periods in which the luminosity in a given band (for instance, in X-rays) exceeds the spin-down power are mainly summarized in Fig. 4.3. There, for a series of models based on varying the initial spin down power of specific pulsars, we computed the maximum efficiency in different bands and the corresponding duration of the superefficiency interval as a function of the pulsar energetics and the minimum radius attained. The efficiencies are larger for the most energetic pulsars, but the duration of these superefficient periods are smaller. Pulsars being more energetic, they are able to sustain the pressure of the medium earlier and their PWNe correspondingly bounce before. The most efficient pulsars are also those attaining the smaller minimum PWNe radii.

The possible existence of superefficient states is in quite general terms independent of model details, since it is based on a conceptual energetic argument in which the

[3] *https://www.isdc.unige.ch/extp/response-files.html*

environment adds energy to the system due to compression, see the previous chapter. However, how large it is (equivalently, which is the amount of maximal compression) will depend on the reality of the assumptions made for the dynamical evolution.

The closest model to ours is that of Gelfand et al. (2009). In particular, regarding the dynamical evolution assumptions both models are comparable. And we notice that they also found large compressions: See, for instance, Figure 2 of Gelfand et al. 2009, in which they show a compression of a PWN by a factor of 16, even when they are considering as baseline the parameters used in Model A in the paper by Blondin 2001, where the L_0 is at the largest level, 10^{40} erg s^{-1} (with other parameters, e.g., ISM medium density, ω, E_{sn}, M_{ej}, etc. being similar to those assumed here). Or see also how these large compressions appear in the case for the PWN CTA 1 as well; see figure 6 of Aliu et al. (2013), where a factor of maximal compression of at least 100 is also shown.

However, we caveat that large compression factors beyond 100 may seem excessive, particularly when compared with hydrodynamical (HD) simulations (see e.g., Bucciantini et al. 2004) and may probably come from model simplifications. We recall that our models are 1-dimensional (thus, spherical, homogenous), which is not generally the case in reality. For instance, Rayleigh-Taylor mixing, see Bucciantini et al. (2004b), Gelfand et al. 2009, activated when the $P_{pwn} > P_{snr}(R_{pwn})$ during free expansion, may later damp coherent compression to this extent. HD and magneto HD simulations of the reverberation period may help understand this dichotomy. However, HD simulations may also be caveated by the fact that the radiative losses of particles are usually not consistently considered (or, simply, not considered at all) in the computation of the PWN pressure. This may lead to an overestimate of the PWN pressure, and thus to diminish the compression factors, since particularly in the reverberation phase, radiative losses of particles can be large. Further analysis are needed to clarify these points.

Interestingly, though, the predictions studied for J1834, on which we also comment below, should not be significantly affected by a reduction of a minimum radius acquired in the reverberation process. This PWN is supposed to be at the start of the reverberation phase, yet far from the maximal compression achievable -a situation that will also be valid in 50 years from now. Also, given the very small duration of the highest-compression regime along the evolution, the duration of the total reverberation process should not change much, if at all. These provide confidence that the simulations results for the number of contracting PWNe should also be in a reasonable range.

Using our models and a Monte Carlo simulation of the youngest 500 pulsars born in our Galaxy, in accordance to population synthesis models, we were able to determine that 1.8 ± 1.3 PWNe should be superefficient today, and at least 16.7 ± 3.8 should be currently contracting. Of course these estimations (as far as we are aware, the first of their class) delineate the ballpark of what is reasonable to expect as a number of contracting

systems in their different phases. Caveats coming from a (still relatively) limited sample of detailed models on which the estimates are based (40 models were studied here), and the model limitations themselves should be bore in mind. In particular, it is useful to note that the assumption of fixing the mass of the ejecta in these PWNe to that of the anchor case used (ultimately done in the lack of better knowledge) may not necessarily turn out to be the best approach in some cases. For instance, models with relatively low L_0 and high ejecta mass (based for instance on G54) might not realize. Being aware of such uncertainty, however, we preferred to have a systematic approach for choosing the PWNe models used.

A direct observational search was also conducted. Analysis of X-ray detections known till now from the *XMM-Newton* Slew Survey did not identify clear candidates of superefficient PWNe. In fact, three interesting sources were signalled in our investigation, but additional observations done with *Swift-XRT* rule them out as possible superefficient PWNe. We concluded that we have probably not detected a superefficient PWNe yet, and that probably none currently exist in the Galaxy (unless of course we are unlucky enough so that a superefficient PWNe lies in the 16% of the sky not covered by the *XMM-Newton* Slew Survey).

However, linked to the reverberation phenomena, superefficient PWNe will inexorably exist in the future. While we wait, reverberation itself can be detected. We have shown this using the specific case of J1834. In less than 10 years from now, we have shown that EPIC pn should be able to tell the difference in flux between the flux measured for this source in 2016 and before and the one obtained then. The latter should be larger, corresponding to the enhancement produced by the contraction. If this is confirmed, we have also shown that such source will become an ideal laboratory for instruments such as *eXTP* and *Athena*, since they will be able to measure the rate of X-ray increase towards superefficiency already in 3-years steps, allowing for a more detailed theoretical comparison.

Chapter 5

Final remarks

5.1 Summary of results and discussion

Using 8.5 years of *Fermi*-LAT data and a contemporaneous ephemeris, we carried out a detailed analysis of PSR J0205+6449 both during its off-peak and on-peak phase intervals. We have used a contemporaenous pulsar ephemeris to gate off its contribution. During the off-peak phases, PSR J0205+6449 / 3C 58 is significantly detected, having a TS value of 202 (i.e., a significance of about 14 σ). This implied a significant increase of the quality of the detection, now undoubtful: we have been able to separate the contribution of the pulsar from that of the nebula. Its spectrum can be modeled by a simple power law. No nebula extension is detected. The flat spectrum and the non-detection of a spectral cutoff also support a PWN origin of the off-peak gamma-ray emission of PSR J0205+6449/3C 58. We have also searched for possible flares in this PWN, which is similar to Crab, of young age and energetic. However, we have found none. The different flux level with Crab hampers a detailed investigation in timescales shorter than 10 days, and the flares -if any- could exist within this duration.

Using the time-dependent model introduced in Chapter 1, where the spin-down power, the particle injection, the energy losses, and the magnetic field all depend on time, and their dependence are accounted for, we have found a good agreement with data considering a nebula at 3.2 kpc (the same distance we use below for the computation of the pulsar magnetospheric power, see Chapter 2) and an age of 2500 years. The magnetic fraction (the fraction of spin-down energy that goes into the magnetic field) for this nebula is relatively high 0.2; thus 3C 58 is a particle-dominated nebula (see Torres et al. 2014). We also noted that there is a degeneracy regarding which inverse Compton contribution dominates at high energies: exploring about a thousand models varying the energy densities and temperatures for the NIR and FIR photon backgrounds we have found, however, that the best fitting set of parameters has similar contributions of both. Forthcoming Cherenkov Telescope Array observations will help determine the peak and

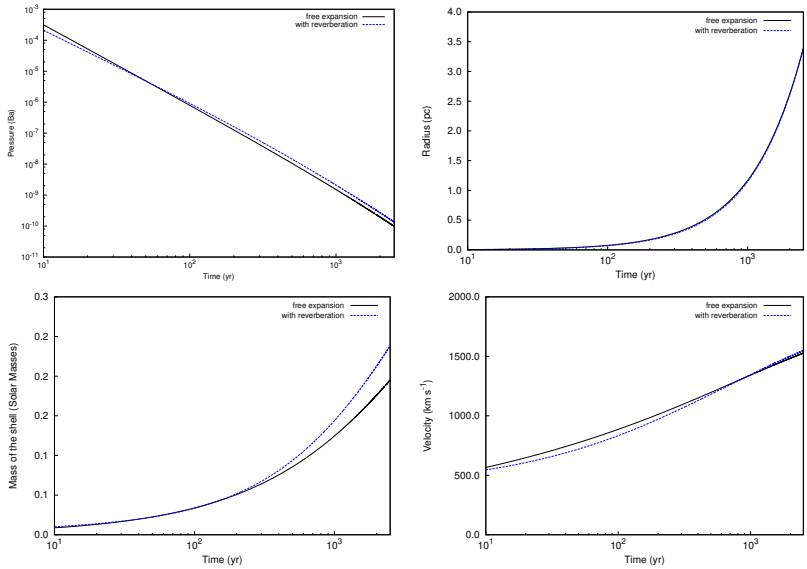

Figure 5.1: Comparison of the evolution of the dynamical variables in models for 3C 58 considering the impact of reverberation, and neglecting it. It is clear that the evolution is essentially unaffected.

the fall-off of the gamma-ray emission, distinguishing between NIR- or FIR-dominated scenarios. For this particular nebula, we have found that reverberation is not yet playing a role in its evolution. In fact, comparing the modelling of the nebula with and without reverberation (i.e., adopting or not reverberation in our code) it can be seen that the differences in the fitting. This is shown in Figure 5.1 below, for the dynamical variables. Only the mass of the shell changes a bit towards the end of the comparison, what is due to the different evolution assumed in the equations of motion. From the dynamical variables of Figure 5.1, one can already argue that the spectral energy distribution will also result the same, as do the fit parameters. The reason is simply that the age of the PWN is too low for reverberation to have an impact, and thus, in order to understand the latter, and characterize it, we have to consider evolving this and other PWNe further, or consider older systems.

To study the reverberation period for a PWN like 3C 58 we have thus to propagate in time the PWN evolution. The specific moment at which reverberation happens is determined by the combined influence of the pulsar and environmental parameters of the system, we found. However, once the current multifrequency data fix all of these, the time evolution is also fixed without the need of additional parameters or assumptions. Fig. 3.1 described above, shows the time evolution of the model fitting the current data for each of the PWNe considered. The two sets of panels show the electron and spectral

energy distributions along time. A strong time evolution is expected. The times shown are chosen within and around the corresponding reverberation period of each PWN, and correspond to the times of the maximum PWN radius, $t_1 = t(R_{max})$, the maximum of the X-ray efficiency, $t_2 = t(\mathrm{Eff}_X^{max})$, the minimum PWN radius, $t_3 = t(R_{min})$, and a later time already at the Sedov phase, $t_4 = t(@Sedov)$. The X-ray efficiency (and correspondingly, radio, GeV, and TeV efficiencies as well) are defined as the ratio of the luminosity emitted in a given frequency range at a given time with respect to the spin-down power at that same time, e.g., $\mathrm{Eff.}_X(t) = L_X(t)/L_{sd}(t)$. If at a time t we measure this ratio to be larger than 1, we have said the PWN is superefficient at that particular energy range. We noted that the X-ray efficiency has several stages of increase and decrease, which can be used to define different phenomenological phases. We called them phases a to c, for reference. We distinguished these phases via the following subsequent events: Phase a has the PWN in free expansion, and lasts from the pulsar birth to the maximum of the nebula radius (at t_1). Phase b finishes at the maximum of the X-ray efficiency (at t_2). Phase c finishes at the minimum of the radius (at t_3). Phase d is the Sedov expansion, assumed to continue after t_3. We see that the the electron distribution is maximum –several orders of magnitude larger- at the start of phase c for the Lorentz factors of interest (e.g., see the curves for Crab from 5800 to 6200 years in the left panel of Fig. 3.3). At the moment of minimum radius, there is just a residual number of electrons at the Lorentz factors needed to emit X-rays in these nebulae (see Fig. 3.1), but they are subject to the strongest magnetic field along the evolution. Thereafter, the re-expansion of the nebula begins and reduces the magnetic field, and since the injection of fresh electrons by the pulsar is slow, for the years to come the efficiency decreases. Only when the new electrons begin to accumulate again the X-ray efficiency recovers. We have shown that supereffiency periods in which the luminosity at a given band from radio to TeV exceeds the pulsar spin-down power, are not only possible, but appear to be common among the PWN evolution: PWNe may have a period in its time evolution where, e.g., the X-ray luminosity exceeds the spin-down power at that time. The difficulty for observing these stages is that they can be maintained only for a few hundred years. Less superefficient PWNe, with maximum X-ray efficiencies in the range of a few hundreds, or a few tens, will have a larger probability to be found, given that they last longer.

In the third work contained in this thesis, in Chapter 4, we have studied, from a more observational perspective, these reverberating and possible superefficient PWNe. First, based on the subsequent evolution of the PWN J1834 we have been able to predict and then simulate its future evolution in time, in case it is indeed starting the reverberating phase as described in our modelling. Maybe a good summary of these latter results is shown in Figure 5.2, where the results of our modelling in time –along a limited time span of 50 years following the current assumed age of J1834- are fitted by simple functions.

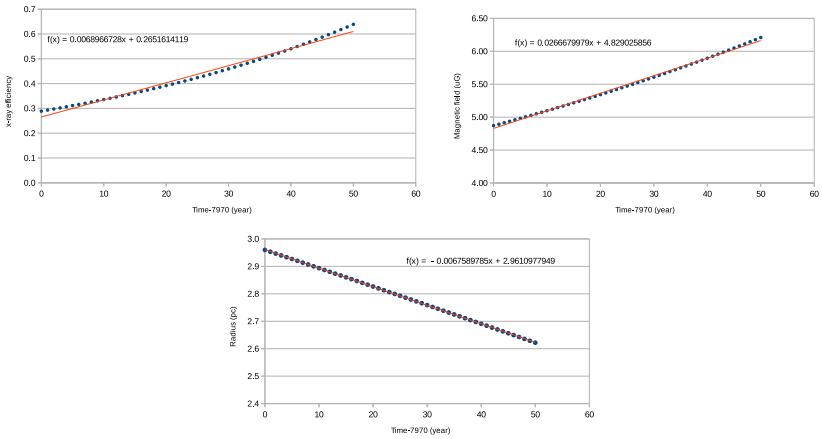

Figure 5.2: Future evolution of dynamical and radiative properties of PWN J1834 in the following years, assuming its current age is around 7970 years.

These are predictions that, as described in more detail in the Chapter 4 above, can be tested in due time, hopefully along contemporaneous' lifetime.

Later, based on a series of systematically studied PWNe models we quantified the duration and significance of the periods of the PWN evolution for which the luminosity in a given band (for instance, in X-rays) exceeded the spin-down power. Our theoretical results were mainly summarized in Fig. 4.3, where, for a series of models based on varying the initial spin down power of specific pulsars, we computed the maximum efficiency in different bands and the corresponding duration of the superefficiency interval as a function of the pulsar energetics and the minimum radius attained. The efficiencies are larger for the more energetic pulsars, but the duration of these superefficient periods are smaller. Pulsars being more energetic, they are able to sustain the pressure of the medium earlier and their PWNe bounce. The more efficient pulsars are also those attaining the smaller minimum PWNe radii. Using these models and a Monte Carlo simulation of the last 500 pulsars born in our Galaxy, in accordance to population synthesis models, we were able to determine that more than a dozen PWN should be reverberating today, and maybe just 1–3 of those are superefficient. These estimations were the first ones done to gather population output of PWNe at this critical evolutionary stage.

5.2 Concluding remarks

Pulsar Wind Nebulae, or plerions, are one of the most important particle accelerators in the Universe and the largest class of identified, Galactic very-high-energy gamma-ray sources (e.g., H. E. S. S. Collaboration, 2018) From observations and simulations, we know

that young PWNe expand freely inside the hosting Supernova Remnant until they reach the reverse shock. When this happens, a compression is usually produced, due to the difference in pressure between the PWN relativistic gas and the SNR shocked medium. When the PWN internal pressure is high enough, the PWN bounces and re-expands again. This phase of contraction and re-expansion of the nebula bubble is called reverberation.

The compression during the reverberation phase causes a strong enhancement of the PWN magnetic field, which may actually burn most of the high-energy electron-positron pairs that produce the characteristic multifrequency spectrum (see e.g., Bucciantini et al. 2011, Vorster et al. 2013, Torres 2017). We have shown that such burning could be so high, that periods in which the luminosity in X-rays or other frequencies exceeds the spin-down power can be found. We characterize this period using an advanced radiative model. However, despite reverberation is a critical phase in the evolution of PWNe, it is usually plainly neglected in dynamical/radiative models, due to the many complexities it entails. Additionally, aspects of the interaction between the reverse showck and PWN shell, or the mass loading at the shell, are very sensitive to some of the environmental parameters and are hardly well-described in full by a set of simplifying assumptions. Thus, a deeper understanding and modelling of the reverberation phase is a key issue in order to characterize the PWN population and correctly determine parameters such as as the age, the pair distribution spectrum, and the photon spectrum, at all subsequent ages beyond. This is nothing but a first effort into such a study. We hope that this thesis will help such works trying to improve on our underlying assumptions in radiative models, combining also, or being informed by, hydrodynamical simulations, which will be ultimately providing a reasonable simulation setup to go through this critical period of evolution.

Bibliography

[1] Abdo, A. A., Ackermann, M., Ajello, M. et al. 2009, ApJL, 699, 102

[2] Abdo, A. A., Ajello, M., Allafort, A., et al. 2013, ApJS, 208, 17 (2PC)

[3] Abdo, A. A., Ackermann, M., Ajello, M. et al. 2013, Science, 331, 739.

[4] Ackermann, M., Ajello, M., Allafort, A. et al. 2013, ApJS, 209, 34 (1FHL)

[5] Aharonian, F., Akhperjanian, A. G., Bazer-Bachi, A. R., et al. 2006, ApJ, 636, 777

[6] Ajello, M., Atwood, W. B, Baldini, L. et al. 2017, ApJS, 232, 18 (3FHL)

[7] Aleksić, J., Ansoldi, S., A., Antonelli, L., A., et al. 2015, JHEAp 5-6, 30-38

[8] Aleksić, J., Ansoldi, S., A., Antonelli, L., A., et al. 2014, A&A, 567, 8

[9] Aliu, E. 2008, in AIP Conf. Ser. 1085, eds. F. A. Aharonian, W. Hofmann, & F. Rieger, 324

[10] Albert, J., Aliu, E., Anderhub, H., et al. 2006, ApJL, 643, L53

[11] Aliu, E., Archambault, S., Arlen, T., et al. 2013, ApJ, 764, 38

[12] Arnaud, M., Ashdown, M., Atrio-Barandela, F. et al. 2016, A&A, 586, 134

[13] Anderhub, H., Antonelli, L. A., Antoranz, P., et al. 2010, ApJ, 710, 828

[14] Atwood, W. B., Abdo, A. A., Ackermann, M., et al. 2009, ApJ, 697, 1071

[15] Bailer-Jones, C. A. L., Rybizki, J., Fouesneau, M., et al. 2018, Astronomical Journal, 156, 58

[16] Bandiera, R. 1984, A&A, 139, 368

[17] Bandiera, R. 2014, Astronomische Nachrichten, 335, 307

[18] Bednarek, W., & Bartosik, M. 2003, A&A, 405, 689

[19] Bednarek, W., & Bartosik, M. 2005, JPhG, 31, 1465

[20] Bietenholz, M. F., Kassim, N. E., Weiler, K. W., 2001, ApJ, 560, 772

[21] Bietenholz, M. F. 2006, ApJ, 645, 1180

[22] Blondin, J. M., Chevalier, R. A., & Frierson, D. M. 2001, ApJ, 563, 806

[23] Bocchino, F., Warwick, R. S., Marty, P. et al. 2001, A&A, 369, 1078

[24] Bucciantini, N., Arons, J., & Amato, E. 2011, MNRAS, 410, 381

[25] Bucciantini, N., Bandiera, R., Blondin, J. M., et al. 2004, A&A, 422, 609

[26] Bucciantini, N., Amato, E., Bandiera, R., et al. 2004, A&A, 423, 253

[27] Buehler, R., Scargle, J. D., Blandford, R. D. et al. 2012, ApJ, 749, 26B

[28] Caliandro, G. A., Hill, A. B., Torres, D. F., et al. 2013, MNRAS, 436, 740

[29] Camilo, F., Stairs, I. H., Lorimer, D. R. et al. 2002, ApJ, 571, L41

[30] Castro, D., Slane, P., Carlton, A., et al. 2013, ApJ, 774, 36

[31] Cerutti, B. Philippov, A. A.; Spitkovsky, A., MNRAS, 457, 2401

[32] Chevalier, R. A., & Fransson, C. 1992, ApJ, 395, 540

[33] Chevalier, R. A. 2005, ApJ, 619, 839

[34] de Jager, O. C., & B*ü*sching, I. 2010, A&A, 517, L9

[35] de Jager, O. C., Raubenheimer, B. C., & Swanepoel, J. W. H. 1989, A&A, 221, 180

[36] Faucher-Giguère, C.-A., & Kaspi, V. M. 2006, ApJ, 643, 332

[37] Fesen, R. A., Rudie, G., Hurford, A., & Soto, A. 2008, ApJS, 174, 379

[38] Gaensler, B. M., & Slane, P. O. 2006, Annu. Rev. Astro. Astrophys., 44, 17

[39] Gaia Collaboration, Brown, A. G. A., Vallenari, A., et al. 2018, A&A, 616, A1

[40] Gehrels, N., Chincarini, G., Giommi, P., et al. 2004, ApJ, 611, 1005

[41] Gelfand, J. D., Slane, P. O., & Zhang, W. 2009, ApJ, 703, 2051

[42] Gelfand, J. D. 2017, Modelling Pulsar Wind Nebulae, 161

[43] Ginzburg V. L., 1979, Theoretical physics and astrophysics. Pergamon Press

[44] Ginzburg V. L., Syrovatskii S. I., 1964, The Origin of Cosmic Rays. Springer

[45] Granot, J., Gill, R., Younes, G., et al. 2017, MNRAS, 464, 4895

[46] Green, D. A. 1986, MNRAS, 218, 533

[47] Gullón, M., Miralles, J. A., Viganò, D., et al. 2014, MNRAS, 443, 1891

[48] Hall, T. A., Wakely, S. P., & VERITAS Collaboration. 2001, in Int. Cosmic Ray Conf., 6, 2485

[49] Hobbs, G., Edwards, R., & Manchester, R. 2006, Chin. J. Astron. Astrophys. Suppl., 6, 189

[50] H. E. S. S. Collaboration, Abramowski, A., Aharonian, F., et al. 2015, A&A, 574, A27

[51] H. E. S. S. Collaboration, Abdalla, H., Abramowski, A., et al. 2018, A&A, 612, A1

[52] Hanabata, Y., Katagiri, H., Hewitt, J. W., et al. 2014, ApJ, 786, 145

[53] Int Zand, J. J. M., Bozzo, E., Qu, J., et al. 2019, Science China Physics, Mechanics, and Astronomy, 62, 29506

[54] Jackson, B., Scargle, J. D., Barnes, D., et al. 2005, ISPL, 12, 105

[55] Kanbach, G., 1999, ApL & C, 38, 17

[56] Kargaltsev O., Pavlov G. G., 2008, in American Institute of Physics Conference Series, Vol. 983, 40 Years of Pulsars: Millisecond Pulsars, Magnetars and More, Bassa C., Wang Z., Cumming A., Kaspi V. M., eds., pp. 171-185

[57] Kargaltsev O., Pavlov G. G., 2010, X-ray Astronomy 2009; Present Status, Multi-Wavelength Approach and Future Perspectives, 1248, 25

[58] Kerr, M. 2011a, PhD thesis, Univ. Washington, arXiv: 1101.6072

[59] Kerr, M. 2011b, ApJ, 732, 38

[60] Kothes, R. 2013, A&A, 560, 18

[61] Kuiper, L., & Hermsen, W. 2015, MNRAS, 449, 3827

[62] Lande, J., Ackermann, M., Allafort, A., et al., 2012, ApJ, 756, 5

[63] Li, J., Torres, D., de Onã Wilhelmi, E., et al. 2016, ApJ, 831, 19

[64] Li, J., Torres, D., Cheng, K.-S.; de Onã Wilhelmi, E., et al. 2017, ApJ, 846, 169

[65] Li, H., & Chen, Y. 2012, MNRAS, 421, 935

[66] Li, J., Rea, N., Torres, D. F., et al. 2017, ApJ, 835, 30

[67] Manchester, R. N., Hobbs, G. B., Teoh, A., et al. 2005, Astronomical Journal, 129, 1993

[68] Martín, J., Torres, D. F., & Rea, N. 2012, MNRAS, 427, 415

[69] Martin, J., Torres, D. F. & Pedaletti, G., 2016, MNRAS, 459, 3868

[70] Meidinger, N., Barbera, M., Emberger, V., et al. 2017, Proceedings SPIE, 103970V

[71] Merloni, A., Predehl, P., Becker, W., et al. 2012, arXiv e-prints, arXiv:1209.3114

[72] Murray, S. S., Slane, P. O., Seward, F. D., Ransom, S. M., & Gaensler, B. M., 2002, ApJ, 568, 226

[73] Pacini, F., & Salvati, M. 1973, ApJ, 186, 249

[74] Pétri, J. 2015, MNRAS, 450, 714

[75] Ray, P. S., Kerr, M., Parent, D., et al. 2011, ApJS, 194, 17

[76] Reynolds, S. P., & Aller, H. D. 1988, ApJ, 327, 845

[77] Roberts, D. A., Goss, W. M., Kalberla, P. M. W., Herbstmeier, U., & Schwarz, U. J. 1993, A&A, 274, 427

[78] Saxton, R. D., Read, A. M., Esquej, P., et al. 2008, A&A, 480, 611

[79] Scargle, J. D., Norris, J. P., Jackson, B., & Chiang, J. 2013, ApJ, 764, 167

[80] Shapiro S. L., Teukolsky S. A., 2004, Black Holes, White Dwarfs and Neutron Stars, Verlag W.-V., ed. Cornell University

[81] Slane, P., Helfand, D. J., Reynolds, S. P., et al. 2008, ApJL, 676, 33

[82] Slane, P., Helfand, D. J., van der Swaluw, E., & Murray, S. S. 2004, ApJ, 616, 403

[83] Slane, P. 2017, Pulsar Wind Nebulae, ed. A. W. Alsabti & P. Murdin, ISBN 978-3-319-21845-8 (Springer International Publishing), 2159

[84] Stephenson, F. R. 1971, QJRAS, 12, 10

[85] Stephenson, F. R., & Green, D. A. 2002, Historical Supernovae and Their Remnants (New York: Oxford Univ. Press)

[86] Strüder, L., Briel, U., Dennerl, K., et al. 2001, A&A, 365, L18

[87] Tanaka S. J. & Takahara F., 2011, ApJ, 715, 1248

[88] Thompson, D. J. 2001, in AIP Conf. Proc. 558, High Energy Gamma Ray Astronomy, ed. F. A. Aharonian & H. J. Volk (Melville, NY: AIP), 103

[89] Tian, W. W., Li, Z., Leahy, D. A., et al. 2007, ApJL, 657, L25

[90] Torres, D. F., Cillis A. N. & Martín J. 2013, ApJ, 763, 4

[91] Torres, D. F. 2017, ApJ 835, 54

[92] Torres, D. F., Cillis A. N., Martín J. & de Oña Wilhelmi 2014, JHEAp, 1, 31

[93] Torres, D. F. 2018, Nature Astronomy, Volume 2, p. 247-256

[94] Torres, D. F., & Lin, T. 2018, ApJL, 864, L2

[95] Truelove, J. K., & McKee, C. F. 1999, ApJS, 120, 299

[96] Uchiyama, Y., Funk, S., Katagiri, H., et al. 2012, ApJL, 749, L35

[97] van den Bergh, S., 1978, ApJ, 220, 9

[98] van den Berg, M., Penner, K., Hong, J., et al. 2012, ApJ, 748, 31

[99] Verner, D. A., Ferland, G. J., Korista, K. T., et al. 1996, ApJ, 465, 487

[100] Vigano, D, Torres, D. F., 2015, MNRAS 449, 3755

[101] Vigano, D, Torres, D. F., & Martin, J. 2015, MNRAS, 453, 2599

[102] Vigano, D, Torres, D. F., Pessah, M., & Hirotani K. 2015, MNRAS, 447, 1164

[103] Vorster, M. J., Tibolla, O., Ferreira, S. E. S., & Kaufmann, S. 2013, ApJ, 773, 139

[104] Weiler, K. W. & Seielstad, G. A., 1971, ApJ, 163, 455

[105] Weiler, K. W., & Panagia, N. 1978, A&A, 70, 419

[106] Wilms, J., Allen, A., & McCray, R. 2000, ApJ, 542, 914

[107] Younes, G., Kouveliotou, C., Kargaltsev, O., et al. 2012, ApJ, 757, 39

[108] Younes, G., Kouveliotou, C., Kargaltsev, O., et al. 2016, ApJ, 824, 138